NASA/TM—2009-215660

Characterization of Triaxial Braided Composite Material Properties for Impact Simulation

Gary D. Roberts and Robert K. Goldberg
Glenn Research Center, Cleveland, Ohio

Wieslaw K. Binienda and William A. Arnold
University of Akron, Akron, Ohio

Justin D. Littell
ATK Space Systems, Inc., Hampton, Virginia

Lee W. Kohlman
University of Akron, Akron, Ohio

September 2009

NASA STI Program . . . in Profile

Since its founding, NASA has been dedicated to the advancement of aeronautics and space science. The NASA Scientific and Technical Information (STI) program plays a key part in helping NASA maintain this important role.

The NASA STI Program operates under the auspices of the Agency Chief Information Officer. It collects, organizes, provides for archiving, and disseminates NASA's STI. The NASA STI program provides access to the NASA Aeronautics and Space Database and its public interface, the NASA Technical Reports Server, thus providing one of the largest collections of aeronautical and space science STI in the world. Results are published in both non-NASA channels and by NASA in the NASA STI Report Series, which includes the following report types:

- TECHNICAL PUBLICATION. Reports of completed research or a major significant phase of research that present the results of NASA programs and include extensive data or theoretical analysis. Includes compilations of significant scientific and technical data and information deemed to be of continuing reference value. NASA counterpart of peer-reviewed formal professional papers but has less stringent limitations on manuscript length and extent of graphic presentations.

- TECHNICAL MEMORANDUM. Scientific and technical findings that are preliminary or of specialized interest, e.g., quick release reports, working papers, and bibliographies that contain minimal annotation. Does not contain extensive analysis.

- CONTRACTOR REPORT. Scientific and technical findings by NASA-sponsored contractors and grantees.

- CONFERENCE PUBLICATION. Collected papers from scientific and technical conferences, symposia, seminars, or other meetings sponsored or cosponsored by NASA.

- SPECIAL PUBLICATION. Scientific, technical, or historical information from NASA programs, projects, and missions, often concerned with subjects having substantial public interest.

- TECHNICAL TRANSLATION. English-language translations of foreign scientific and technical material pertinent to NASA's mission.

Specialized services also include creating custom thesauri, building customized databases, organizing and publishing research results.

For more information about the NASA STI program, see the following:

- Access the NASA STI program home page at *http://www.sti.nasa.gov*

- E-mail your question via the Internet to *help@sti.nasa.gov*

- Fax your question to the NASA STI Help Desk at 443–757–5803

- Telephone the NASA STI Help Desk at 443–757–5802

- Write to:
  NASA Center for AeroSpace Information (CASI)
  7115 Standard Drive
  Hanover, MD 21076–1320

NASA/TM—2009-215660

Characterization of Triaxial Braided Composite Material Properties for Impact Simulation

Gary D. Roberts and Robert K. Goldberg
Glenn Research Center, Cleveland, Ohio

Wieslaw K. Binienda and William A. Arnold
University of Akron, Akron, Ohio

Justin D. Littell
ATK Space Systems, Inc., Hampton, Virginia

Lee W. Kohlman
University of Akron, Akron, Ohio

Prepared for the
65th Annual Forum and Technology Display
sponsored by the American Helicopter Society
Grapevine, Texas, May 27–29, 2009

National Aeronautics and
Space Administration

Glenn Research Center
Cleveland, Ohio 44135

September 2009

Level of Review: This material has been technically reviewed by technical management.

Available from

NASA Center for Aerospace Information
7115 Standard Drive
Hanover, MD 21076–1320

National Technical Information Service
5285 Port Royal Road
Springfield, VA 22161

Available electronically at http://gltrs.grc.nasa.gov

Characterization of Triaxial Braided Composite Material Properties for Impact Simulation

Gary D. Roberts and Robert K. Goldberg
National Aeronautics and Space Administration
Glenn Research Center
Cleveland, Ohio 44135

Wieslaw K. Binienda and William A. Arnold
University of Akron
Akron, Ohio 44325

Justin D. Littell
ATK Space Systems, Inc.
Hampton, Virginia 23681

Lee W. Kohlman
University of Akron
Akron, Ohio 44325

Summary

The reliability of impact simulations for aircraft components made with triaxial braided carbon fiber composites is currently limited by inadequate material property data and lack of validated material models for analysis. Improvements to standard quasi-static test methods are needed to account for the large unit cell size and localized damage within the unit cell. The deformation and damage of a triaxial braided composite material was examined using standard quasi-static in-plane tension, compression, and shear tests. Some modifications to standard test specimen geometries are suggested, and methods for measuring the local strain at the onset of failure within the braid unit cell are presented. Deformation and damage at higher strain rates is examined using ballistic impact tests on 61- by 61- by 3.2-mm (24- by 24- by 0.125-in.) composite panels. Digital image correlation techniques were used to examine full-field deformation and damage during both quasi-static and impact tests. An impact analysis method is presented that utilizes both local and global deformation and failure information from the quasi-static tests as input for impact simulations. Improvements that are needed in test and analysis methods for better predictive capability are examined.

Introduction

A wide range of materials, fiber architectures, and manufacturing methods are available to make carbon fiber composite components for fixed wing aircraft, rotorcraft, and the engines that power these vehicles. For some potential new application, the use of textile reinforcements and resin infusion processes offer the opportunity to meet performance requirements at a cost that is comparable with current technology. A recent development is the use of composite materials in fan cases for jet engines. Approaches using triaxial braided preforms with various resin infusion processes have been developed for this application. To achieve airworthiness certification, a full-scale engine blade-out test must be performed to demonstrate that the fan containment system can contain a released fan blade and that the fan case can maintain sufficient structural integrity to survive the large dynamic loads imparted by the unbalanced rotor during spool down. Blade and case deformation during a fan blade-out event can usually be simulated with sufficient accuracy using commercial explicit finite element codes.

Fragmentation of the fan blade and failure of the case can also be simulated for engines that utilize traditional metallic blade and case materials. The accuracy of the simulations currently achievable for metallic systems is the result of having an adequate material database and having a large experience base for correlation of analysis with test results during development and certification of many engines that are currently in service. There is much less material data available and very limited experience with such correlation for fan containment systems that utilize composite fan cases. The ultimate goal of current research is to improve the blade-out simulation capability for composite fan cases to a level comparable to that achievable for metallic cases. The work presented in this report is a first step toward that goal. Modifications to standard test methods that are needed to characterize the type of triaxial braided composites that are being utilized for composite fan cases are investigated, and a computationally efficient method for representing the braid architecture in impact simulations is presented. An important objective is to coordinate test and analysis method development so that tests performed for material characterization can also yield material property data in a form that is needed for composite material models used in the analysis. Ballistic impact tests were performed on composite panels in a way that approximates the impact velocity, deformation mode, and strain energy density at failure for composite material in a fan case during blade-out. These impact test results are used for test and analysis correlation.

Standard test methods for measuring quasi-static, in-plane material properties were used as much as possible in this work. A summary of common test standards for continuous-fiber reinforced polymer matrix composites can be found in ASTM D4762 (Ref. 1). Guidance for textile composite materials can be found in ASTM D6856 (Ref. 2). Additional guidance can be found in the Composite Materials Handbook, DOD–MIL–HDBK–17/1F (Ref. 3). Issues related to airworthiness certification are presented by Tomblin (Ref. 4). Specific issues related to 2×2 biaxial braided composite materials made by resin transfer molding (RTM) have also been considered by Tomblin (Ref. 5). There is little guidance available for testing of composites with two-dimensional triaxial braid architecture. A useful series of papers related to testing of triaxial braided composites has been published by Masters et al. (Refs. 6 to 9). These papers primarily consider issues such as specimen geometry and strain gage size needed to measure global material properties, although there is some discussion of localized deformation. Papers that explore non-uniform deformation in various textile composites have been published, and papers focused on the triaxial braid architecture are beginning to appear in the literature. A summary of some of these papers and a description of an approach using digital image correlation methods to examine local deformation in triaxial braided materials can be found in Littell (Ref. 10). Littell describes test methods that were developed specifically for composites with a two-dimensional triaxial braid architecture that utilizes large-tow-size (12k and 24k), flattened carbon fibers. The large unit cell size of this material presents some challenges for measuring material properties using standard composite test methods. Non-uniform deformation and edge-initiated damage can cause unrealistic failure modes that result in measured values for stiffness and strength that are not representative of the material as it would be used in a structure. This report explores the effects that non-uniform deformation and edge damage can have on measured stiffness and strength of triaxial braided composites when standard tension, compression, and shear test methods are used. Alternative specimen geometries that mitigate these effects are presented. Smaller scale local deformation and damage within the braid unit cell is also examined.

At the minimum, quasi-static material property data are required to perform an impact analysis. A fully accurate representation of material deformation and failure requires additional data at strain rates representative of the impact event. A limited amount of work has been done on development of high-strain-rate test methods, and research in this area continues. This report focuses on developing the framework for a coordinated test and analysis approach using quasi-static data, but the methodology will be able to use high-strain-rate data as test methods are developed and the data become available. Results from earlier ballistic impact tests on composite panels have been used to provide information about

potential failure modes for various material systems, and a wide variety of failure modes were observed. It is clear from this experimental data that fiber/matrix interface failure will have to be added to the analysis methods presented in this report to fully represent the behavior of these materials. However, some of the materials did not exhibit much fiber/matrix failure during impact. For these systems, failure initiates as a local fiber fracture and propagates as cracks along the directions of axial or bias fiber bundles within the braid. This report focuses on a material system of this type and discusses a computationally efficient approach for impact simulation that is capable of simulating the effect of braid architecture on crack propagation.

There has been a significant amount of research conducted in the analysis and modeling of textile composites. The majority of the efforts have concentrated on various means to determine the effective mechanical properties of woven materials. Among the earliest attempts to model these materials was that of Chou and Ishikawa (Ref. 11). In their original mosaic model, the woven composite was approximated as a one-dimensional series of laminated cross-ply composites, and classical laminate theory in combination with isostress or isostrain assumptions were applied to obtain the effective stiffness properties of the material. They later extended the model to account for the fiber undulations that are present in an actual woven material. This approach was extended to two dimensions in work by Naik and Shembekar (Ref. 12), in which a mixture of parallel and series assumptions were applied to obtain the effective properties of the material. To analyze more complicated fiber architectures such as braided composites, researchers such as Pastore and Gowayed (Ref. 13) and Byun (Ref. 14) modeled the fibers as a series of rods at various angles, and utilized simple isostrain assumptions to obtain the overall effective properties of the composite. More sophisticated analysis methods, such as those developed by Tanov and Tabiei (Ref. 15) and Bednarcyk and Arnold (Ref. 16), used an approach where a representative unit cell of a woven composite was created, and then micromechanics-based approaches were applied to compute the effective properties and response of the material. In the context of applying these methods within a finite element model, elements are created with a homogenized set of material properties, and the appropriate analysis method is used to generate the effective properties and response of the woven material.

The analytical methods mentioned above use homogenized elements, which do not directly take into account the architecture of the textile material within a finite element model. However, to simulate the directionality of cracking observed for some triaxial braided composites, the braid architecture should be directly simulated within the finite element model. To account for the fiber architecture in a computationally efficient manner, Cheng (Ref. 17) developed an approach where the braid architecture is modeled as a series of layered shell elements where each element is a laminated composite with the appropriate fiber layup. The effective stiffness and strength of the equivalent unidirectional composite were then included as input data for the finite element analysis. In the method developed by Cheng, fiber and matrix properties were combined using simple micromechanics-based approaches to obtain the required effective properties. The model was developed within the context of LS–DYNA (Ref. 18), a commercially available transient dynamic finite element code commonly used within the aerospace industry. A continuum damage mechanics-based composite constitutive model available within LS–DYNA was used as the material model.

In the work described in this report, two major extensions to the approach developed by Cheng (Ref. 17) have been made. First, the discretization of the braid has been adjusted to account for the relative positions of the axial braid fibers in different layers of the multi-ply composite. More significantly, a method has been developed to derive the required material property data directly from tests of the triaxial braided material. In the previous approaches, the effective unidirectional composite properties of the materials utilized in a braided composite either had to be measured experimentally or computed using micromechanics techniques. This approach requires an additional experimental program, with tests on either the matrix constituent (for micromechanics approaches) or tests on “equivalent” unidirectional composites made from the same fibers used for the braided composite. This is a significantly larger experimental effort. There is an additional concern that the properties of the

matrix and the properties of the equivalent unidirectional composite do not accurately represent the in situ properties of the matrix material and fiber bundles within the braided composite because of processing differences required to fabricate the matrix and unidirectional specimens. Furthermore, if micromechanics-based approaches are directly applied within the analysis model, the computational cost can be increased significantly. In the approach to be described in this report, the equivalent unidirectional properties of the composite are calculated from properties of the braided composite. With this approach, in situ properties are used for the material model. In addition, the computational efficiency of the simulations is significantly increased because there is no need to incorporate micromechanics methods into the analysis through some sort of local-global approach.

Materials

The composite materials that are currently of most interest for engine fan cases are made by resin infusion processes using two-dimensional triaxial braided preforms and 177 °C (350 °F) cure epoxy resins. Many fiber/matrix combinations have been investigated. This report will focus on results obtained using TORAYCA T700S fiber (Toray Carbon Fibers America, Inc.) and CYCOM PR 520 matrix (Cytec Industries, Inc.). T700S is a high strength, standard modulus carbon fiber. PR520 is a one-part toughened resin specifically designed for the RTM process. Results obtained using the T700S/PR520 material system will be presented for the purpose of demonstrating issues related to test method development and implementation of test data in impact analysis. Some additional results will be presented using the same fiber and EPIKOTE Resin 862/EPIKURE Curing Agent W matrix (Resolution Performance Products, now Hexion Specialty Chemicals). This matrix material is a two-part, low-viscosity system that is easy to process because of its low viscosity and long working life at room temperature. This resin system will be called E–862 in this report. The processing characteristics of this system were useful for fabricating single-layer composite panels that are described later.

The two-dimensional triaxial braided preforms were made by A&P Technology, and composite panels were fabricated by resin transfer molding (RTM) at North Coast Composites. A [0°/+60°/–60°] triaxial braid architecture was used. A picture of the preform and a representative unit cell are shown in Figure 1.

In Figure 1 the ±60° bias fibers are visible on the surface. Portions of the 0° axial fibers that lie below the ±60° bias fibers can be seen in the open spaces between the ±60° bias fibers. The 0° axial fibers were 24k flattened tows while the ±60° bias fibers were 12k flattened tows. Although larger fiber bundles were

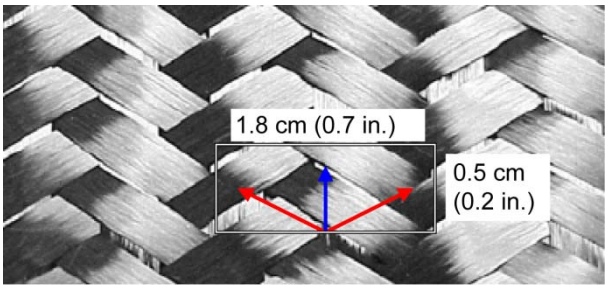

Figure 1.—Two-dimensional triaxial braided carbon fiber preform with highlighted unit cell (blue arrow indicates axial fiber direction, and red arrows indicate bias fiber directions).

used in the axial direction, the fiber bundle spacing in the axial and bias directions were adjusted to give the same fiber volume in the axial and bias directions. This is a quasi-isotropic in-plane fiber architecture, so the global in-plane stiffness is expected to be the same in all directions when the region of interest includes several unit cells of the braided material.

Composite panels were fabricated by placing six layers of the [0°/+60°/–60°] braided preform into the RTM mold with the 0° fibers aligned in the same direction. Although the axial (0°) fibers in the various layers were aligned, the lateral position of the axial tows in the six layers was random. Resin was injected into the closed mold and cured according to processing conditions recommended by the resin manufacturer. Cured panel dimensions (after trimming) were 0.6096 m (2 ft) wide by 0.6096 m (2 ft) long by 0.3175 cm (0.125 in.) thick. Fiber volume of the cured composites was measured using the acid digestion technique. The T700S/PR520 composite had a fiber volume of 55.9 ± 0.18 percent. Single-layer composites were also fabricated using the T700S/E–862 material system. When a laminated composite is made from unidirectional plies, a balanced laminate must be fabricated to avoid warping. It was possible to fabricate flat single-layer panels with no warping using the triaxial braid because the [0°/+60°/–60°] braid architecture is quasi-isotropic and all fiber directions are contained within a single layer of braid. However, if pieces of material cut from the panel contain less than a unit cell, these smaller pieces of material would have a significant twist. The single-layer specimens used for this work contained at least one unit cell in the gage sections, so the test specimens were flat.

Quasi-Static Tests

Standard test methods have been developed that rely on having a uniform deformation field in the gage section of the test specimen in order to accurately measure in-plane tension, compression, and shear properties. Results of tests on materials with a triaxial architecture like that in Figure 1 have indicated that modifications to standard test methods are needed because the large fiber bundle size and large unit cell size can result in non-uniform deformation within the gage section and within the unit cell. In addition, premature failure resulting from edge effects can result in failure modes for the coupon that cause artificially low strength measurements. To examine the limitations of current test methods, tests on the triaxial braided composites were performed using standard methods for measuring properties in tension (Ref. 19), compression (Ref. 20), and shear (Refs. 21 and 22). Specimens were tested in a hydraulically actuated, 220-kN (50-kip) test machine under displacement control with a displacement rate of 0.635 mm/min (0.025 in./min).

One difference from the standard methods was the use of digital image correlation methods to measure full-field strain instead of using strain gages or extensometers. A commercial image correlation system was used. Load measurements from the test rig were input to the image correlation system to generate stress-strain curves. The digital image correlation technique is similar to that described by Littell (Ref. 10). A brief summary is provided here. Two cameras are connected to a computer equipped with software capable of pattern recognition and calculation of position from stereo images. A calibration procedure is performed in which a series of images of known dimensions are placed in the intersecting field of view of the two cameras, and the location of the image is mapped by the software. This results in a calibrated volume of space that can be used for tracking displacement of test specimens under load. The test specimen is painted with a speckle pattern for optimum pattern recognition. A three-dimensional map of the specimen surface is obtained before the specimen is loaded. The specimen is then loaded, and the pattern recognition software is able to track the three-dimensional displacement of any point that remains in the initial field of view. Strain is then calculated from surface displacements measured at specified time intervals during a test. Stress-strain curves are calculated from the synchronized load and strain measurements.

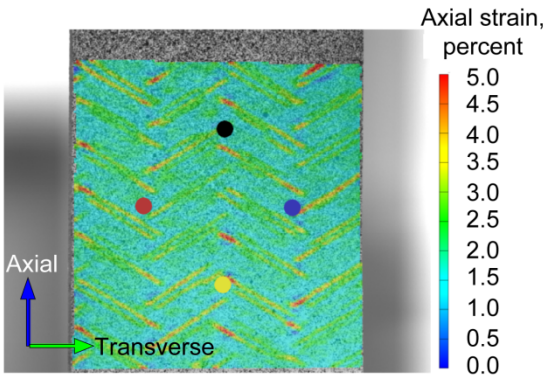

Figure 2.—Typical axial strain field in axial tensile test. Colored dots indicate points used for global strain calculations in axial and transverse directions.

Figure 2 shows an example of the axial strain field measured at one specific time step during an axial tensile test. The field of view in Figure 2 captures the entire 3.578-cm (1.409-in.) specimen width and approximately 5.08 cm (2 in.) of the specimen height. The strain field in Figure 2 is non-uniform and shows high-strain regions within the braid architecture that can become sites for local damage. An average strain can be calculated by averaging the non-uniform strain within a particular field of view or by tracking the location of specific points. A potential problem with the averaging approach is that the calculated strain can be affected by unrealistically high strain values and possible loss of pattern recognition at local damage sites. To avoid this complication, global strain was measured by tracking specific points that are separated by a distance that is large compared with the size of the local damage. The locations of these points, which are approximately 1.905 cm (0.75 in.) apart, are indicated in Figure 2. The two points aligned along the specimen vertical axis are used to calculate axial strain, and the two points aligned along the specimen horizontal axis are used to calculate transverse strain. Global strains are calculated by dividing the relative displacement between the two points in the loaded condition by their original separation in the unloaded condition. This is later referred to as an "optical strain gage."

Tests were performed to measure tension, compression, and shear properties in axial and transverse directions. In the axial tests, the axial braid fibers (blue arrow in Fig. 1) are aligned along the load direction. In the transverse tests the axial braid fibers are aligned perpendicular to the load direction. The full-field strain measurements were used during all of these tests to examine the uniformity of the strain field and to attempt to identify local deformation and damage within the braid unit cell.

Compression Test Results

Compression tests were performed according to methods described in ASTM D3410 (Ref. 20). Test specimens were 91cm (6.0 in.) long by 3.58 cm (1.41 in.) wide. These dimensions allowed for a long gripped region with a short 2.54-cm (1.00-in.) gage section as specified by the standard test method. The width was selected to include at least two unit cells. For an axial test, the width includes two unit cells, and the length of the gage section includes five unit cells. For a transverse test, the width includes seven unit cells, but the length of the gage section includes less than one and a half unit cells. At least two unit cells in the gage length would be preferred, but the longer gage length required to include two unit cells in the transverse test is not desirable because it increases the possibility of buckling.

Figure 3 shows the results of compression tests for the T700S/PR520 material system. A representative full-field strain map for a T700S/PR520 axial compression specimen is shown in Figure 3(a). The deformation in Figure 3(a) is homogeneous with no perceptible effect of the braid architecture. The deformation observed in transverse compression tests was also homogeneous. The failure mode for a T700S/PR520 axial compression specimen is shown in Figure 3(b). The failure occurs in the middle of the gage section, and there is no evidence of premature failure resulting from edge

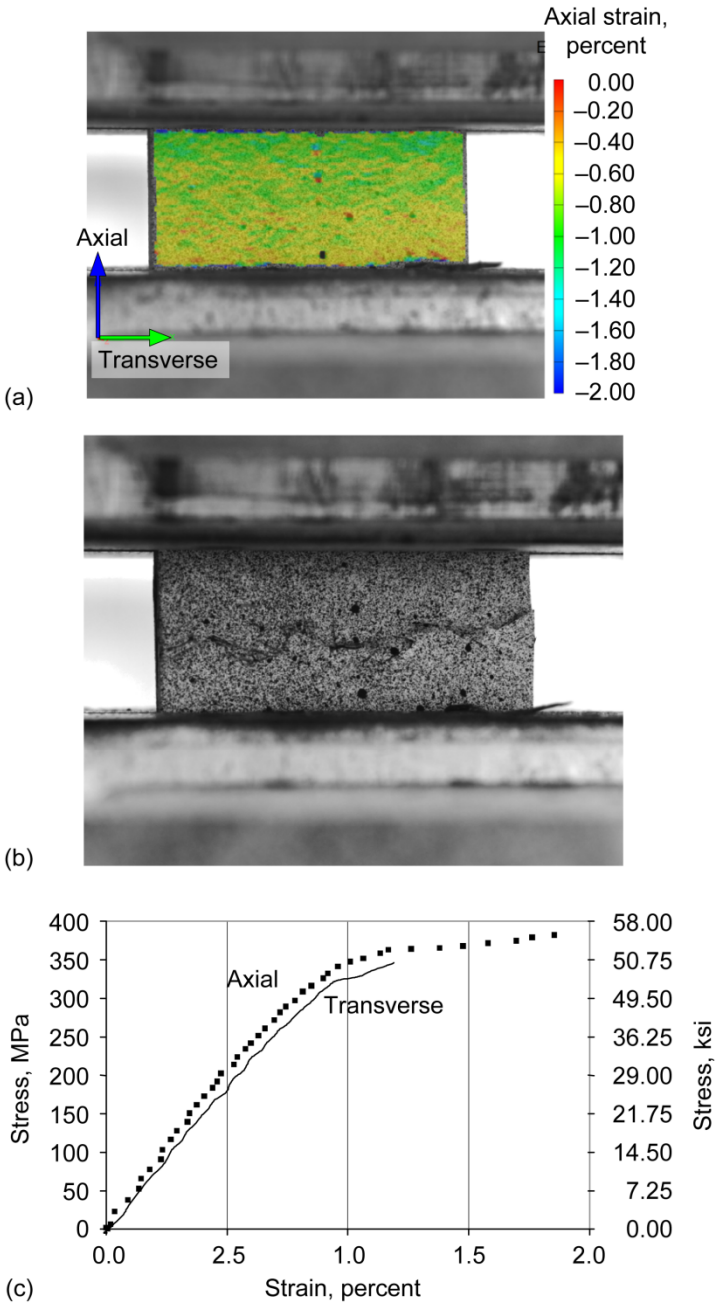

Figure 3.—Results of typical compression tests for T700S/PR520 material system. (a) Axial compression test specimen showing uniform axial strain field. (b) Gage section failure of axial compression test specimen. (c) Axial and transverse compression stress-strain curves.

effects. Full-field strain measurements indicated that there were no problems with misalignment or buckling in these tests. Similar results were observed for the transverse compression tests. Since the deformation is homogeneous and there appears to be no edge effects, the standard test method for compression appears to be adequate for measuring compression properties of the triaxial braided composites when a toughened matrix like PR520 is used and there is good fiber/matrix bonding. There is some evidence (not reported here) that failure might be influenced by edge effects when more brittle matrix materials are used or there is poor fiber/matrix bonding. Further investigation of the strain field near failure is continuing in order to evaluate the possible influence of edge effects on failure stress and strain for T700S/PR520 and other material systems. Typical axial and transverse compression stress-strain curves for T700S/PR520 are shown in Figure 3(c). Only two tests were performed for each orientation to determine average material properties because of limited material availability. Additional testing is planned when materials become available. Compression test results are shown in Table I for the two material systems reported in this work.

TABLE I.—COMPRESSION PROPERTIES

Material (fiber/resin)	Axial direction			Transverse direction		
	Strength, MPa (ksi)	Modulus, GPa (Msi)	Failure strain, percent	Strength, MPa (ksi)	Modulus, GPa (Msi)	Failure strain, percent
T700S/PR520	378 (54.8)	41.9 (6.08)	1.80	346 (50.2)	39.0 (5.66)	1.10
T700S/E–862	327 (47.4)	41.4 (6.00)	1.01	303.5 (44.0)	42.7 (6.19)	0.87

Shear Test Results

Two standard test methods commonly used for measuring shear properties of composite materials are ASTM D5379, “V-Notched Beam Method” (Ref. 21) and ASTM D7078, “V-Notched Rail Shear Method” (Ref. 22). The V-Notched Beam Method is also commonly referred to as an Iosipescu Shear Test. A triaxial braided test specimen fabricated to the geometry used for the D5379 test method is shown in Figure 4(a). In this test method the load is applied through the edges of the specimen. Since the fixtures for this type of loading were not available in our laboratory, the specimen was loaded through the faces as shown in Figure 4(b). Red and dark blue regions in Figure 4(b) are areas where high local strain causes failure prior to failure in the gage region. This damage can propagate into the gage area and influence both the shape of the stress-strain curve and the measured failure strength.

The standard specimen geometry used for the D7078 V-Notched Rail Shear Method is shown in Figure 5(a), and a modified specimen design developed in this work is shown in Figure 5(b). Advantages of the D7078 method are discussed in Reference 23. For the triaxial braid architecture investigated in this work it was found that some edge damage can occur along the 45° edge between the notch and the clamps. To overcome this limitation, the modified “H” specimen geometry shown in Figure 5(b) was developed and used for this work. Details about the development of this modified shear test will be published elsewhere. Figure 6 shows a failed T700S/PR520 specimen held by one of the specimen grips after a test. Figure 7 shows the horizontal strain and shear strain distributions in the gage area of an “H” specimen immediately before failure.

In Figure 7, the shear deformation is located mostly within the gage area. The width of the deformation region is similar to the notch width of 0.7 cm (0.28 in.). In Figure 7 the axial braid fibers are horizontal, and there is about one unit cell within the width of the deformed area. A test specimen with vertical orientation of axial braid fibers would have about one-third of a unit cell within the width of the deformed region. The effect of unit cell size relative to the size of the deformation area needs to be further examined in order to establish the validity of the test method for determining global shear properties. The regions of red and dark blue are damaged areas resulting from termination of fiber bundles at specimen edges. Modifications of the notch size and shape are being considered to reduce these edge failures. The strain near the center of the gage area was calculated over an area that is approximately 0.3 by 0.3 mm (0.012 by 0.012 in.). Different averaging techniques were used and shown to have very little effect on the measured value, though further investigation is needed to develop a standard method for analyzing and

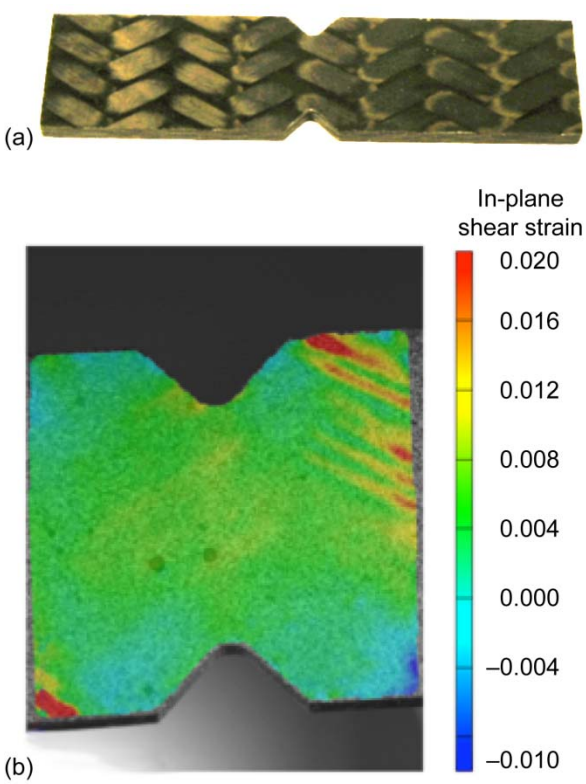

Figure 4.—Test specimen geometry defined by ASTM D5379 V-Notched Beam Method (Ref. 21). (a) Triaxial braid shear test specimen. (b) In-plane shear strain field.

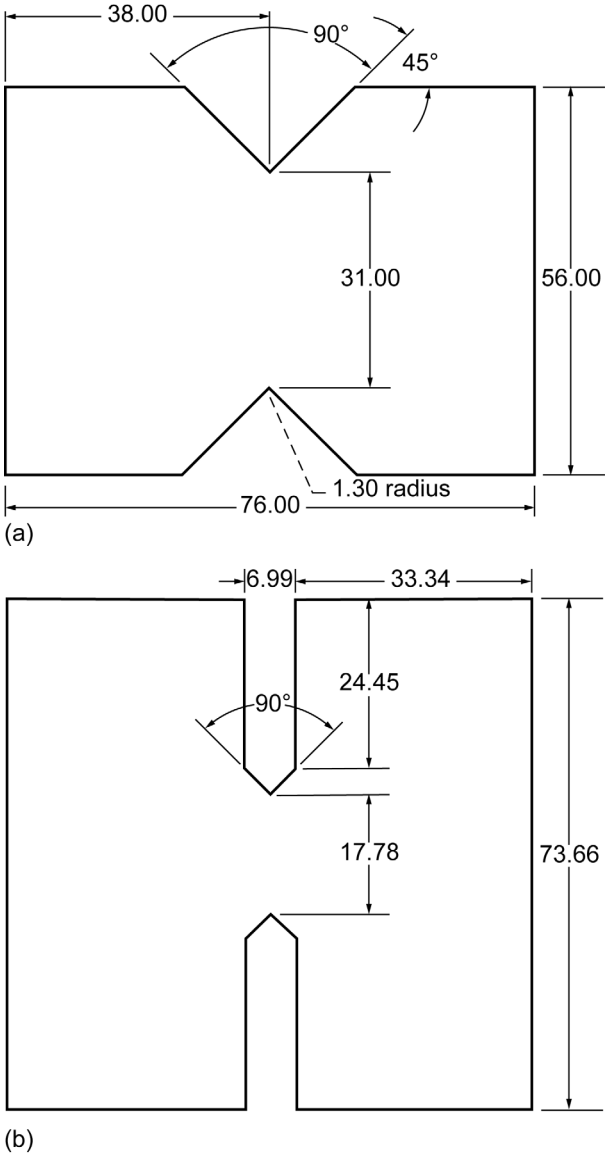

Figure 5.—Test specimen geometry for the ASTM D7078 V-Notched Rail Shear Method (dimensions in millimeters). (a) Standard. (b) Modified.

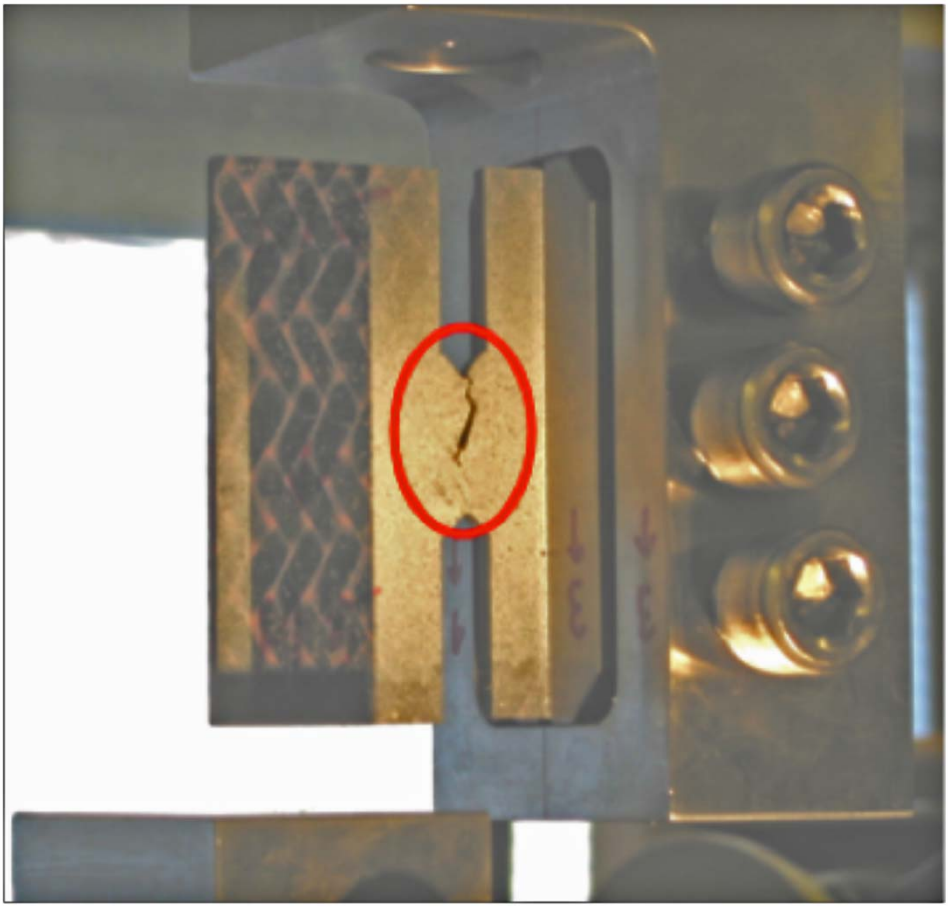

Figure 6.—Modified “H” specimen after failure with left grip removed to view crack.

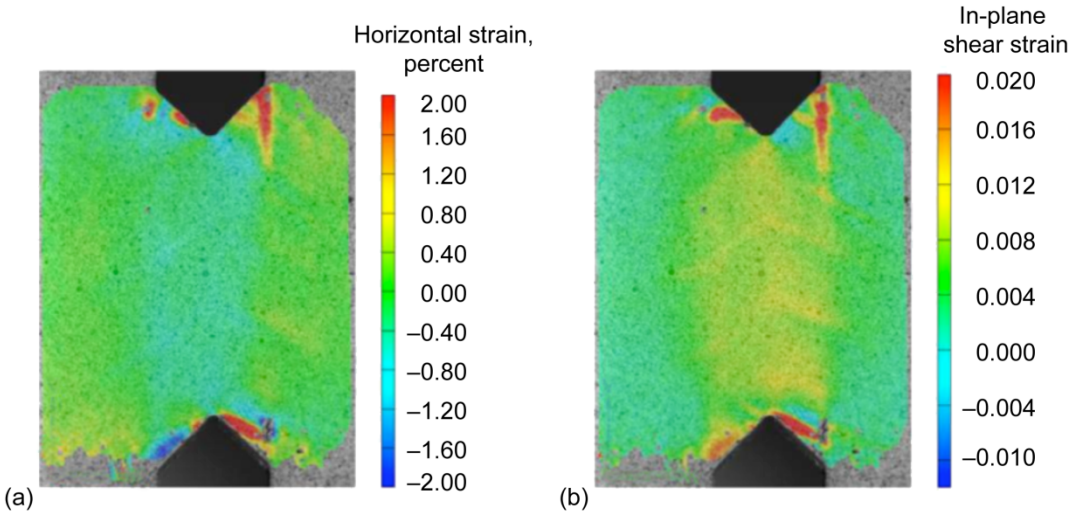

Figure 7.—T700S/PR520 test specimen of modified “H” geometry for strain measurements using ASTM D7078 V-Notched Rail Shear Method. (a) Horizontal strain. (b) Shear strain.

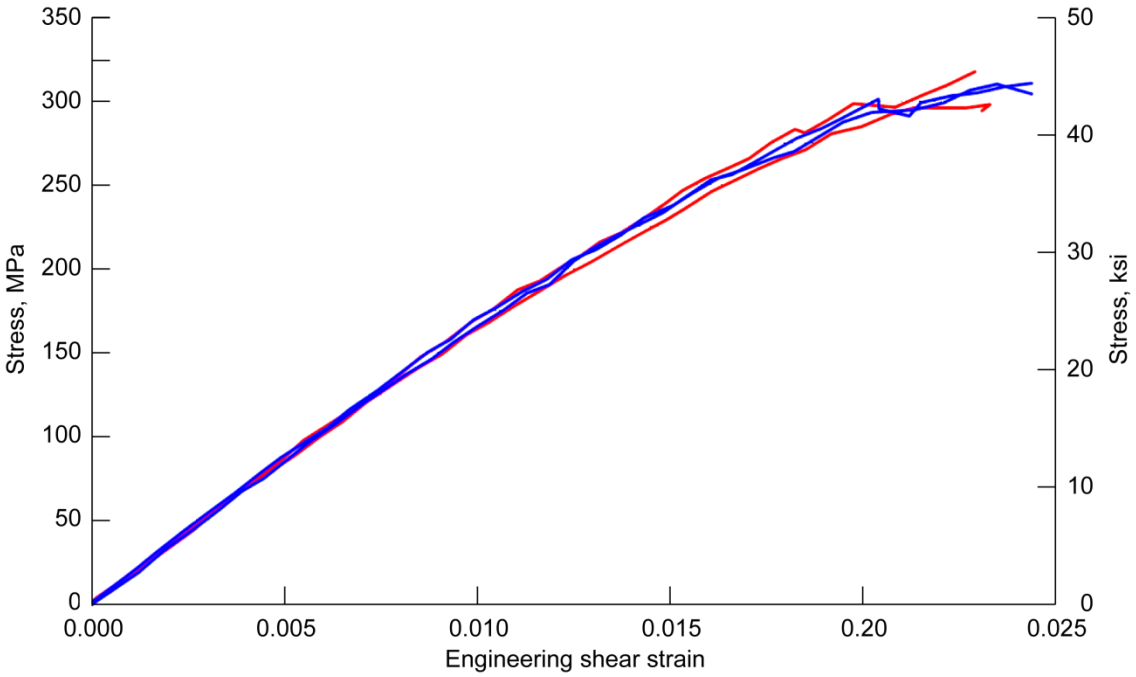

Figure 8.—Shear stress-strain curves for T700S/PR520. Red curves correspond to axial braid fibers horizontal in Figure 7. Blue curves correspond to axial braid fibers vertical in Figure 7.

TABLE II.—SHEAR PROPERTIES[a]

Material (fiber/resin)	Strength, MPa (ksi)	Modulus, GPa (Msi)	Failure strain, percent
T700S/PR520	309±8 (44.8±1.2)	17.5±0.3 (2.53±0.04)	2.24±0.06
T700S/E–862	256±12 (37.1±1.7)	16.2±0.5 (2.34±0.07)	1.98±0.14

[a]Error limits represent one standard deviation.

extracting the desired values from the full-field strain results. The shear stress-strain curves are shown in Figure 8. The shear properties are nearly the same in the axial and transverse orientations.

Table II shows T700S/PR520 shear properties obtained as averages from the four curves in Figure 8. Similar data are shown in Table II for the T700S/E–862 material system. The shear modulus was measured as the slope between 0 and 0.2 percent strain. Strength and failure strain were taken at the last measured point before failure, which was defined as a sudden significant (usually greater than 25 percent) decrease in load (most specimens) or the point at which the curve shows no further load increase. Table II and Figure 8 include a clarification of data presented in a previous report (Ref. 24). Here, the calculated shear modulus is based on “engineering” shear strain rather than “tensorial” shear strain, as in the previous report. The calculated shear modulus in Table II is the correct value to use for the analyses described in this report. Analysis results in this report differ slightly from those in Reference 24 because of this difference in definition of shear strain.

Tensile Test Results

The strain fields observed in the compression and shear tests presented above were nearly homogeneous. The effect of the braid architecture on the uniformity of the strain field within the gage area and within the unit cell was small, and in many cases not detected at all. In contrast, the strain field in tensile test specimens showed effects of the braid architecture within the entire gage area and within the unit cell. The pattern of the ±60° bias fibers on the surface of the specimen is clearly visible in Figure 2. The non-uniform strain field has been investigated for various material systems and discussed in detail in

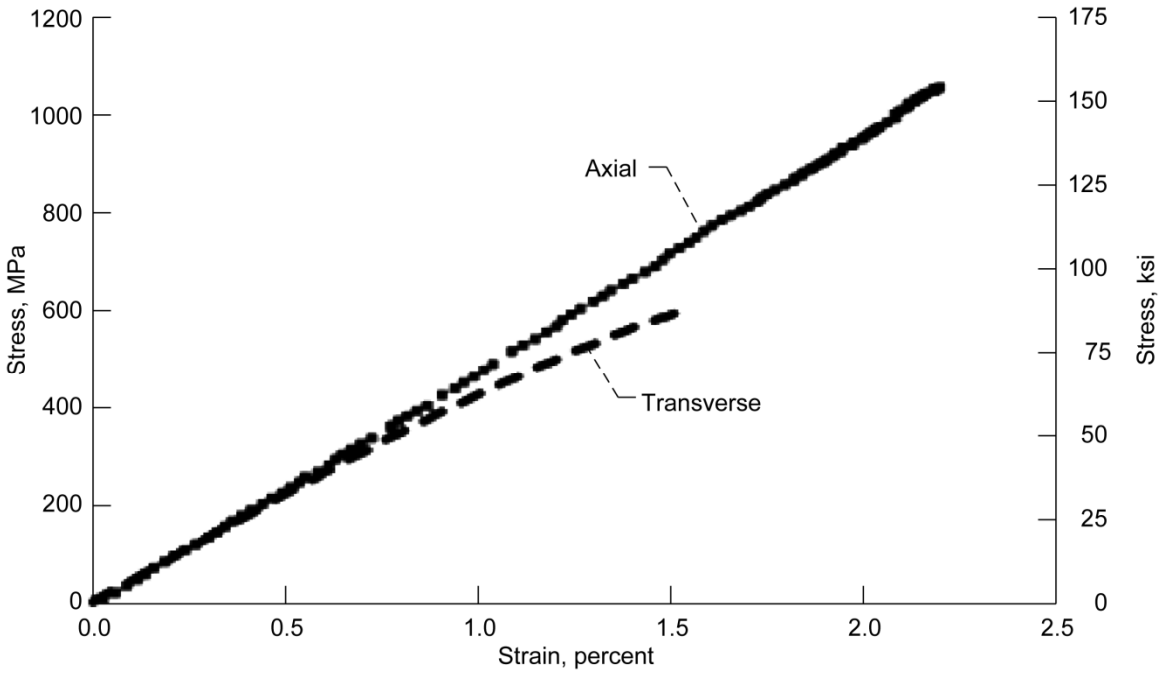

Figure 9.—Global stress versus global strain for T700S/PR520 from axial and transverse tensile tests.

TABLE III.—COMPOSITE MATERIAL TENSILE PROPERTIES[a]

Material (fiber/resin)	Axial direction				Transverse direction			
	Strength, MPa (ksi)	Young's modulus, GPa (Msi)	Failure strain, percent	Poisson's ratio	Strength, MPa (ksi)	Young's modulus, GPa (Msi)	Failure strain, percent	Poisson's ratio
T700S/PR520	1035±34 (150±4.9)	47.6±1.1 (6.9±0.2)	2.16±0.09	0.31±0.02	599±3 (87±0.4)	42.8±1.6 (6.2±0.2)	1.68±0.19	[b]0.30±0.003
T700S/E–862	800±6 (116±0.9)	46.9±1.6 (6.8±0.2)	1.78±0.08	0.30±0.03	462±36 (67±5.2)	41.6±1.3 (6.0±0.2)	1.44±0.09	0.29±0.02

[a] Error limits indicate one standard deviation.
[b]Average value for two tests.

Reference 10. Some results from Reference 10 are reviewed in this section, and additional test results using single-layer composite specimens are reported.

Straight-sided tensile test specimens were prepared in accordance with ASTM D3039. Specimens of 30.48 cm (12 in.) length by 3.578 cm (1.409 in.) width were used for the tensile tests. These dimensions were chosen so that the width contained at least two unit cells and the length conformed to the ASTM D3039 length-to-width ratios. Typical axial and transverse tensile test results for T700S/PR520 specimens are shown in Figure 9. Five measurements were performed for each material system. Average measured properties are shown in Table III.

Premature failure near fiber bundles that terminate at free edges can influence the shape of the stress-strain curve and the measured failure strain. A large amount of edge damage was observed in both axial and transverse tensile tests. In an axial tensile test the axial braid fibers lie along the specimen axis and are gripped on both ends during a test. Since these axial braid fibers carry most of the load, the reduction in strength caused by edge damage is small for the axial tensile test. The axial tensile stress-strain curve shown in Figure 9 is therefore linear until failure. The edge damage has a larger effect on the measured strength for the transverse tensile test because all of the axial braid fibers are perpendicular to the applied load. There is no continuous load path between the grips through fibers because all axial and bias fiber bundles terminate at a free edge. The edge damage contributes to the nonlinearity of the transverse tensile

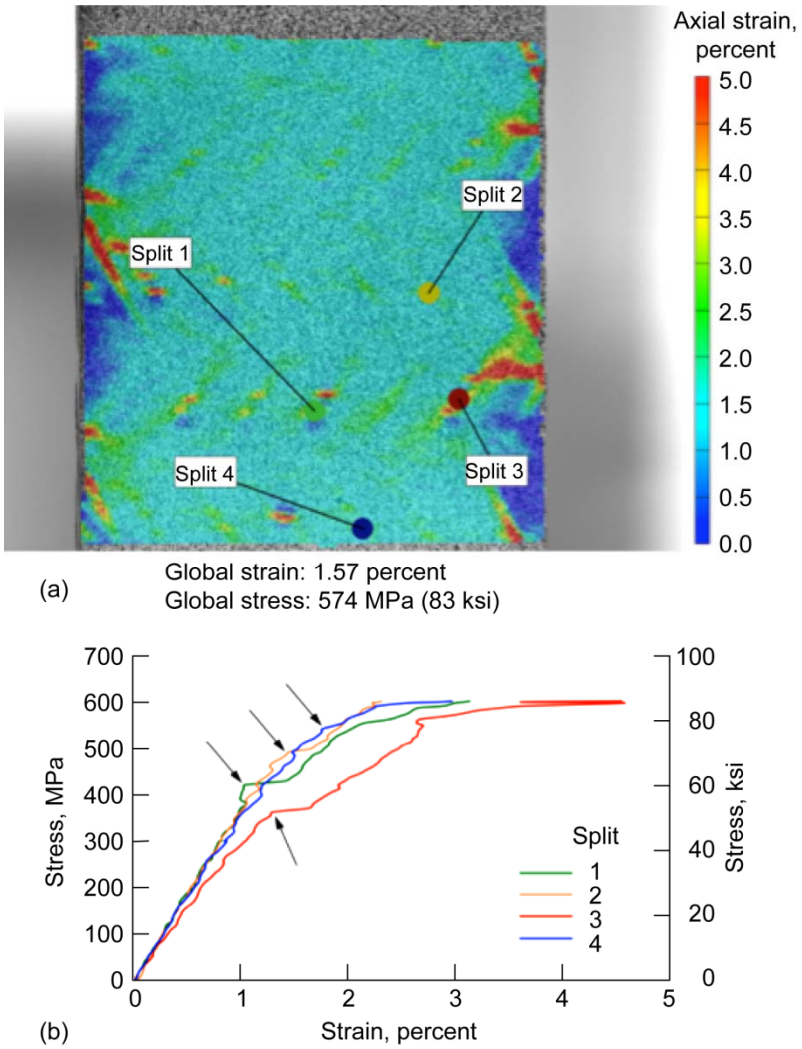

Figure 10.—Transverse tensile test results for T700S/PR520. (a) Full-field strain data. (b) Global stress versus local strain plot.

stress-strain curve in Figure 9 and also contributes to the reduced transverse failure stress compared with the axial failure stress.

Figure 10 shows the edge damage and other localized damage that occurs during a transverse tensile test. The axial strain field in a specimen loaded close to failure is shown in Figure 10(a). Global stress versus local strain is shown in Figure 10(b) for the four locations indicated by points in Figure 10(a). The dark blue triangular regions near the edges of the specimen in Figure 10(a) are regions of low strain that are not carrying load because of edge damage. Here, the edge-damaged region is about 10 percent of the specimen width. Since the damaged region does not carry load, the stress in the undamaged region is about 10 percent higher than the stress that is calculated based on the initial cross-sectional area of the specimen. The transverse stress-strain curve in Figure 9 is therefore not an accurate representation of the transverse tensile properties. In addition to the edge damage, localized damage is visible as small horizontal lines throughout the specimen in Figure 10(a). These local regions of high strain occur as a result of splitting in the subsurface axial braid fiber bundles, which lie in a horizontal direction in Figure 10(a). The locations of the first four splits that occur are indicated by colored dots. The local strain in the regions of these fiber bundle splits can be measured for each time step in the test. Figure 10(b) shows the global stress versus local strain curves for the four split locations. The global stress versus local

strain curves are similar to the transverse global stress versus global strain curve in Figure 9 up to about 1 percent strain. The curves in Figure 10(b) show an abrupt increase in local strain at the locations indicated by arrows. These abrupt increases are associated with splitting of the subsurface axial braid fiber bundles. The strain at which the abrupt increase occurs can be considered to be the in situ transverse fiber bundle failure strain for the axial braid fiber bundles. This is a useful material property for analysis if it is assumed that the failure strain measured on the surface is the same as the failure strain for interior plies. Some support for this assumption was found through microscopic examination of the interior of specimens, which had been loaded to strains lower than the failure strain. Edge view images of specimens that were cut and polished indicated that the extent of fiber bundle splitting is similar for all plies.

Single-Ply Test Methods

Specimens used to obtain the test results in the previous section were made from composite panels with six plies of triaxial braid. The axial fibers were aligned for all plies, but the transverse positioning of the plies was random. The full-field strain results presented above show some of the effects of the braid architecture for a surface ply that is constrained by the remaining five plies. Single-ply composites were fabricated and tested in order to focus more directly on the deformation within an unconstrained unit cell of the braid. The T700S/E–862 material system was used for making the single-ply laminates because of material availability and the ease of processing this resin system. Testing of single-ply shear and tensile specimens is ongoing; details of the test methods and more extensive results will be published elsewhere. However, some preliminary results that are relevant to issues discussed above are reported in this report.

The out-of-plane displacement for a single-ply transverse tensile specimen is shown in Figure 11. The red and yellow regions in Figure 11 represent displacements out of the plane of the image. The dark and light blue regions represent displacements into the plane of the image. This local bending at the specimen edges is periodic with spacing dictated by the braid architecture. Similar, but much smaller, out-of-plane deflection occurs in the six-ply laminates. This indicates that stresses associated with out-of-plane displacement can contribute to the edge damage observed in the six-ply tests. The axial strain in the same single-ply T700S/E–862 straight-sided transverse tensile specimen is shown in Figure 12. Figure 12(a)

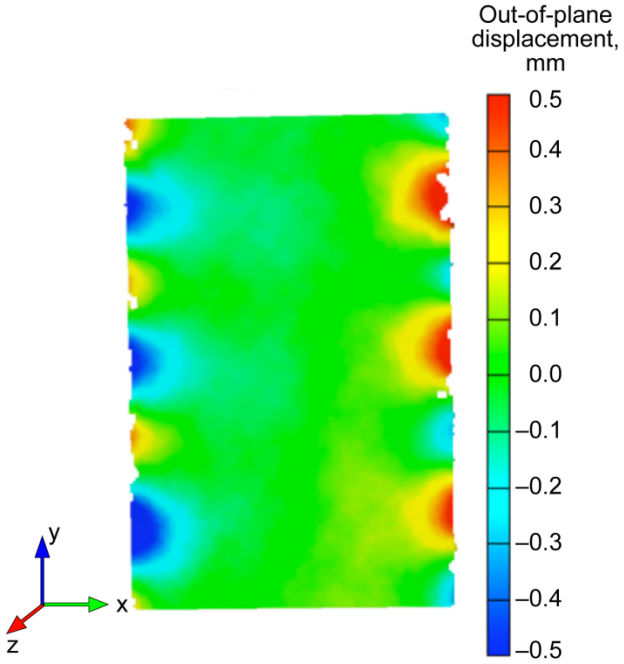

Figure 11.—Out-of-plane displacement for single-layer T700S/E–862 transverse tensile specimen.

shows the full-field axial strain measurements, and the associated stress-strain curve is shown in Figure 12(b). Areas of high (red) and low (blue) strain correspond to areas of high out-of-plane deformations shown in Figure 11. Axial fiber bundle splitting (similar to that shown in Fig. 10(a)) can also be seen as red dots throughout the specimen. Further work is being performed to compare the onset of this type of damage in single- and six-ply T700S/E–862 straight-sided specimens. Figure 12(b) shows the global stress versus global strain curve for this specimen, which was obtained using a 2.5- by 2.5-cm (1- by 1-in.) optical strain gage.

The fiber bundle splits in Figures 10(a) and 12(a) are characteristic of the material, but the edge damage is an artifact of the test method. A bowtie specimen geometry has been proposed to eliminate edge effects and provide more reliable strength measurements, particularly for the transverse tensile strength (Ref. 25). This specimen was shown to give transverse tensile strengths much higher than those measured using standard straight-sided specimens. The reliability of stress-strain measurements obtained using this type of specimen is investigated here using a single-ply test specimen. Figure 13 presents the axial strain results for a T700S/E–862 single-ply bowtie specimen. The axial strain measured during a transverse tensile test is shown in Figure 13(a). Figure 13(b) shows the global stress versus global strain curve obtained using a 6.23- by 6.23-mm (0.25- by 0.25-in.) optical strain gage centered in the specimen notch.

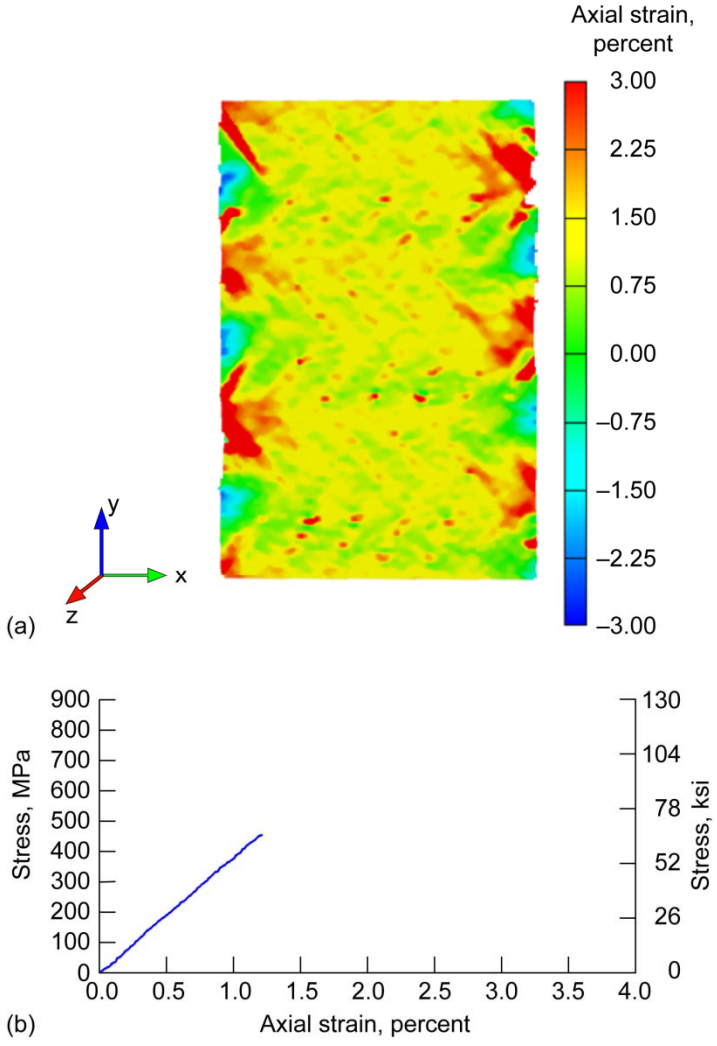

Figure 12.—Axial strain for T700S/E–862 single-ply straight-sided transverse tensile specimen. (a) Full-field strain. (b) Global stress versus percent global strain curve.

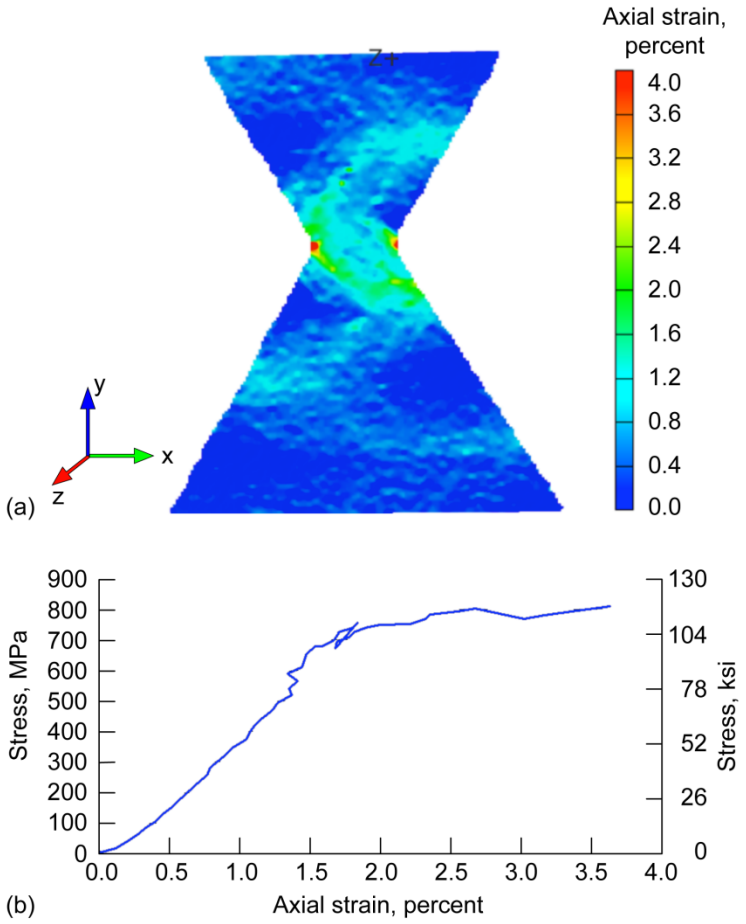

Figure 13.—Axial strain for T700S/E–862 single-ply bowtie transverse tensile specimen. (a) Full-field axial strain. (b) Global stress versus percent global strain in gage area.

The red color in Figure 13(a) is high deformation at the notch. The notch effect seems to be blunted when the first continuous bias fiber is encountered. It is therefore possible that the notch has little effect on strength. The strain field in the region between the notches is somewhat uniform, although efforts are continuing to optimize the specimen geometry for a more uniform strain field in the gage area. Since the stress-strain curve for the bowtie specimen (Fig. 13(b)) is similar to the curve for the straight-sided specimen (Fig. 12(b)) in the linear region, it might be possible to design a bowtie specimen that could be used for stiffness as well as strength measurements. The straight-sided specimen has an abrupt failure at a strain of about 1.2 percent and stress of 450 MPa (65.27 ksi). The bowtie specimen shows a more gradual failure and higher failure stress of approximately 800 MPa (116 ksi).

Impact Tests

Ballistic impact testing was performed using a single-stage compressed gas gun to propel a soft projectile into 61-cm (24-in.) by 61-cm (24-in.) by 3.2-mm (0.125-in.) composite panels. The composite panel is held in a 5.1-cm- (2-in.-) wide steel picture frame fixture with a 51- by 51-cm (20- by 20-in.) aperture. The projectile is a mixture of gelatin and phenolic microballoons. The composition is similar to that of projectiles commonly used to simulate bird strikes on aircraft. The molded projectile is a cylinder with a length of 12.7 cm (5 in.), a diameter of 7.0 cm (2.75 in.), and a nominal density of 0.92 g/cm^3. A

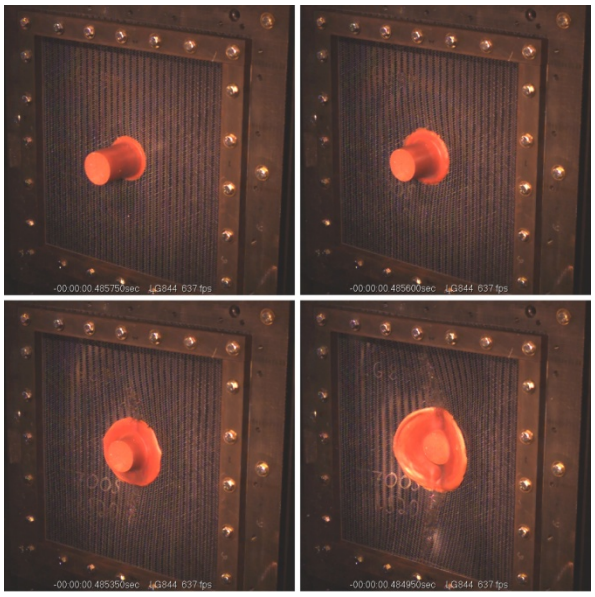

Figure 14.—Panel impact test configuration, illustrating deformation of gelatin projectile during impact.

soft projectile was used rather than a hard projectile because the objective was to induce a high strain energy density in the composite material before failure. The impact test configuration showing the deformation of the projectile during a typical test is shown in Figure 14.

Tests are performed over a range of impact velocities to determine the velocity for onset of damage, the growth of damage with increasing velocities, the penetration threshold, and the damage pattern induced by penetration. The penetration velocity depends on the material system, but velocities above 500 ft/s are common for the more impact resistant material systems. Further information about the test method can be found in Reference 26. More recent information about current high-speed video capabilities and the digital image correlation methods used are discussed below.

Typical data acquisition consisted of multiple high-speed digital video cameras in various locations. Recording rates were typically on the order of 10 000 to 20 000 frames per second with speeds up to 60 000 frames per second at reduced resolution for special interest tests. Panel displacement and strain data is measured using a digital image correlation system that is similar to the one described above except that pairs of high-speed cameras are used instead of the lower speed cameras that are used for quasi-static tests. Full-field strain maps are collected for each time step in the high-speed video. Typical data calculated for this work include out-of-plane displacement, strain in the vertical direction (approximately equal to material axial strain), and strain in the horizontal direction (approximately equal to material transverse strain). In Figure 15, a deflection pattern is shown as an overlay on an image of the back of a panel during impact for a typical impact test.

Six T700S/PR520 panels were impacted using impact velocities ranging from 122 to 230 m/s (400 to 756 ft/s). The lowest velocity impact produced no visible damage, and the highest impact velocity completely penetrated the panel. The threshold velocity for penetration was between 191 m/s (627 ft/s) and 194 m/s (637 ft/s). The onset of fiber failure on the backside of the panel occurred between 183 m/s (601 ft/s) and 186 m/s (609 ft/s). There was no fiber failure for an impact velocity of 183 m/s (601 ft/s). Figure 16 shows the front and back of the panel impacted at 186 m/s (609 ft/s). Figure 17 shows a closeup view of the damage at the center of the initial contact area on the back of the panel. The paint on the back

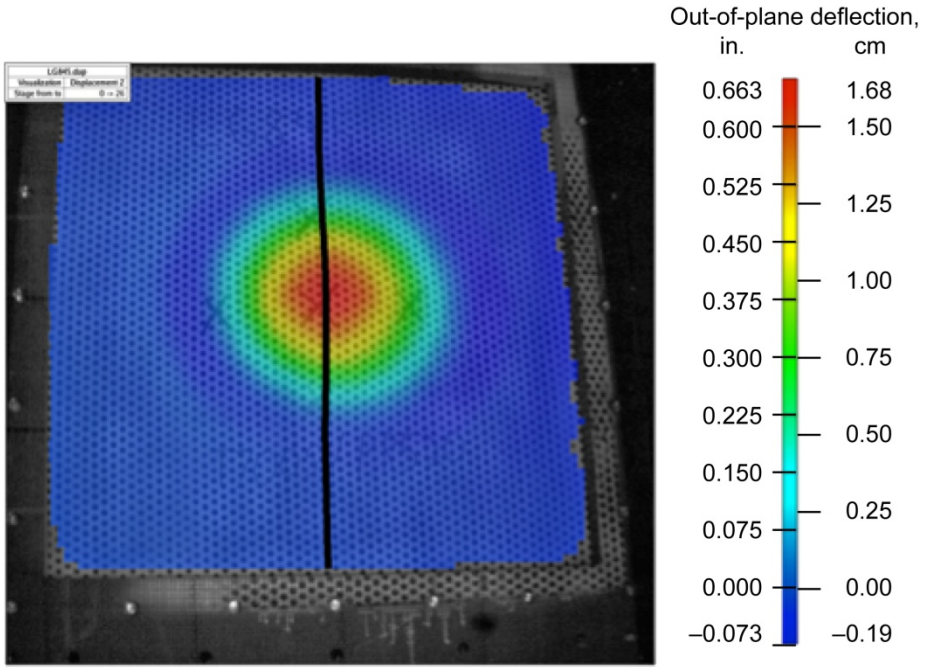

Figure 15.—Typical deflection pattern during composite panel impact test.

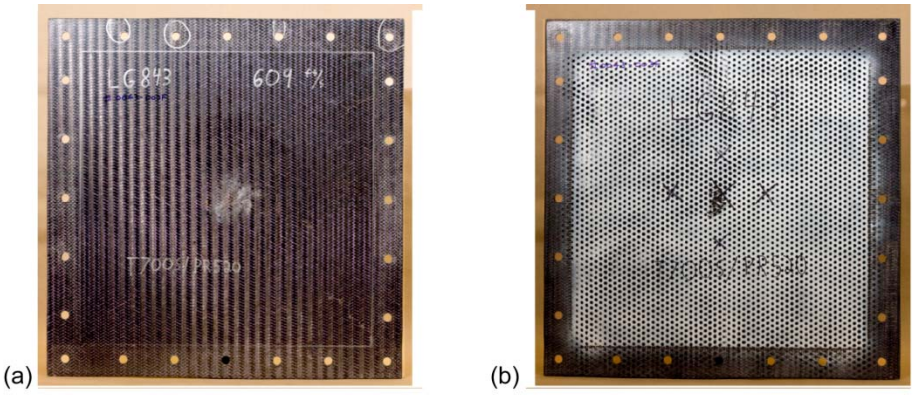

Figure 16.—T700S/PR520 panel after impact at 186 m/s (609 ft/s). (a) Front. (b) Back.

of the panel was used to provide a pattern for deformation measurements by digital image correlation. Both axial and bias fibers show some tensile failure. Surrounding the region of tensile failure there is evidence of transverse splitting within the fiber bundles, similar to the splitting that was observed in the quasi-static tensile tests. The impacted panels are currently being examined by ultrasonic through transmission and thermography to check for nonvisible damage.

The displacement of any point on the back of the panel can be determined by digital image correlation, as illustrated in Figure 18. Figure 18(a) shows the out-of-plane displacement versus position for points that lie along a vertical line (located as shown in Fig. 15) that passes through the center of the panel during an impact test at 186 m/s (609 ft/s). Curves are shown for the first seven video frames after initial contact of the projectile on the panel. Figure 18(b) shows the horizontal (transverse) strain corresponding to the curves in Figure 18(a). Regions of high strain correspond to regions of high deformation because the strain is caused primarily by the local curvature of the panel.

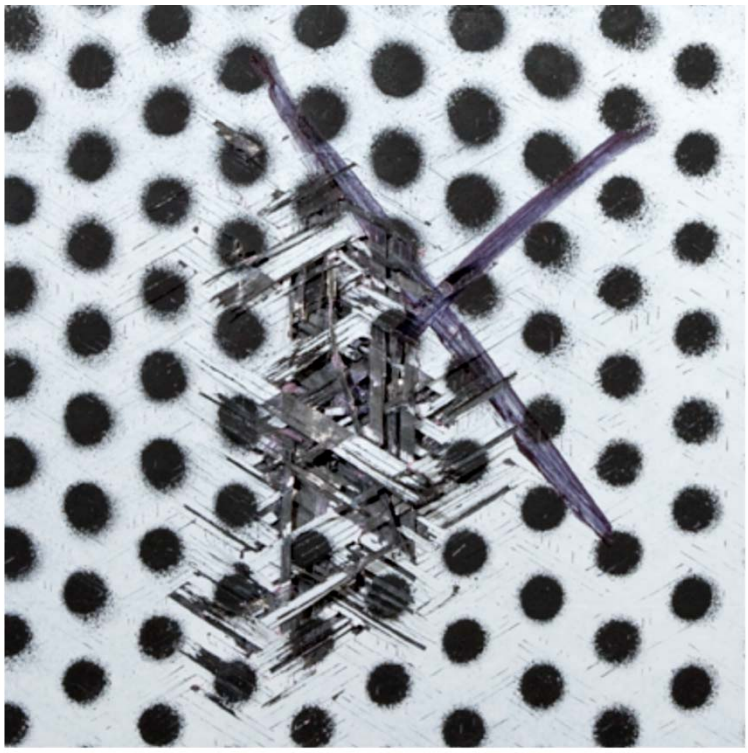

Figure 17.—Closeup image of damaged area on back of T700S/PR520 panel in Figure 16 after impact at 186 m/s (609 ft/s).

The discontinuity at the peak of the curves in Figure 18 indicates that fibers have fractured. The paint pattern used for image correlation is lost when fiber fracture occurs, and deformation can no longer be measured in that region of the panel. The time interval between frames in this example is 37 μs. Since the video frames are not synchronized with the initial contact of the projectile on the panel, the time after initial contact corresponding to the curves in Figure 18 is only known within 37 μs. The deflection of the panel at 148±37 μs after initial impact is 1.32 cm (0.52 in.) and the strain at the same time is 1.4 percent. Fiber failure appears to initiate at a deflection slightly greater than 1.32 cm (0.52 in.) and a strain slightly greater than 1.4 percent. The transverse tensile strain at failure reported in Table II for the quasi-static tensile test using straight-sided specimens was 1.69±0.19. The failure strain measured in the quasi-static and impact tests are similar. However, there is a large uncertainty in the quasi-static test result (i.e., ±0.19 for one standard deviation), and the exact strain at failure can only be estimated from the impact test because the 37 μs time step is too long to ensure that the last unbroken curve in Figure 18(b) corresponds to a time just before failure. It is also recognized that the impact test involves multiaxial loading, out-of-plane deformation, and high strain rates, so the failure strains measured in the quasi-static tests are not expected to be equal to the failure strains measured during impact.

In addition to the high tensile strain at the center of the panel, there is a negative (compressive) strain with a maximum value of –0.25 percent in a circular region outside of the central region of maximum deflection (see Figs. 15 and 18(b)). This is a result of negative curvature of the panel in this region. There is no evidence of compressive failure in the impact test. This is consistent with the quasi-static compressive failure strain of 1.10 percent indicated in Table I, and the linearity of the compression stress-strain curve up to a strain of 1.0 percent in Figure 3(c).

An impact test performed at 191 m/s (627 ft/s) showed similar, but more extensive, fiber fracture on the back of the panel. A closeup image of the failure region is shown in Figure 19. A test performed at 194 m/s (637 ft/s) resulted in penetration of the panel by the projectile. Figure 20 is a sequence of frames

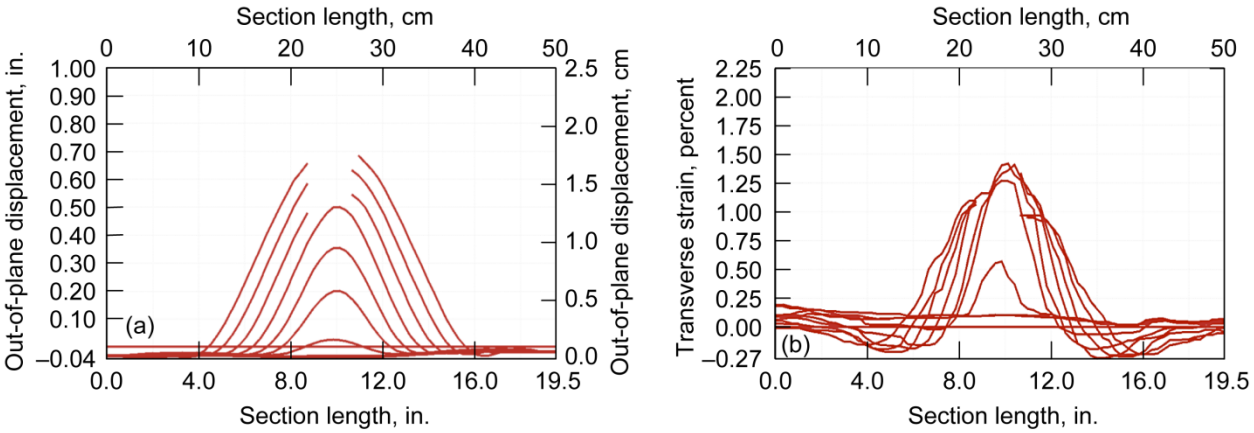

Figure 18.—Impact of panel in Figure 16 for locations along vertical line as shown in Figure 15. (a) Out-of-plane displacement. (b) Transverse strain.

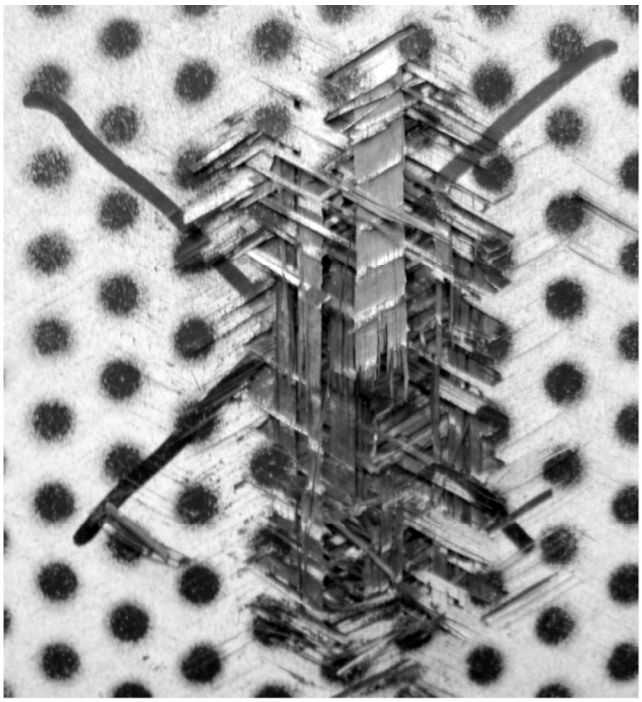

Figure 19.—Closeup image of damaged area on back of T700S/PR520 panel after impact at 191 m/s (627 ft/s).

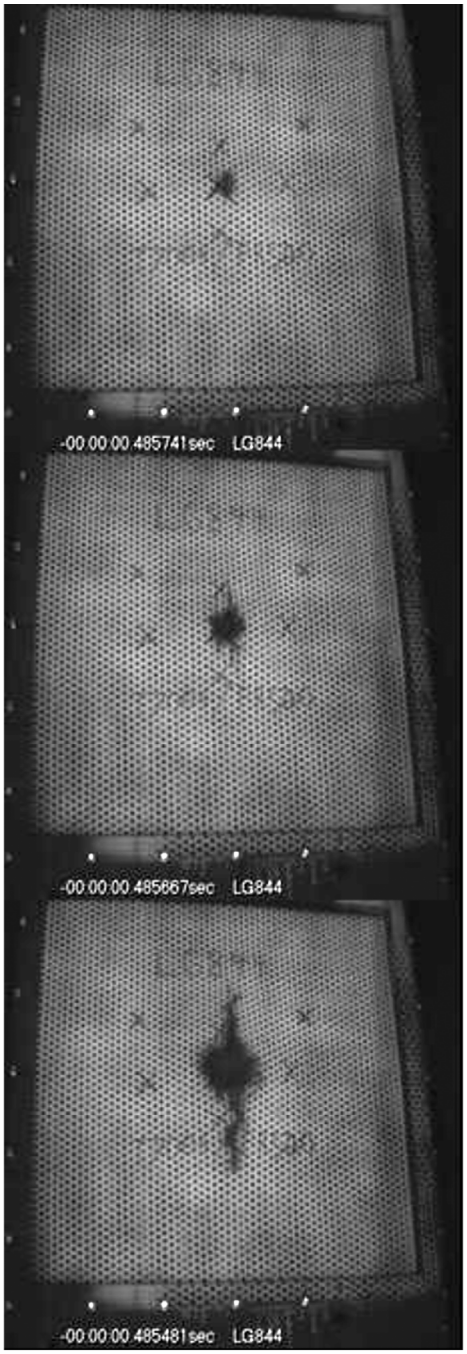

Figure 20.—Frames from high-speed video of T700S/PR520 panel impacted at 194 m/s (637 ft/s) showing first fiber failure, crack initiation, and crack propagation.

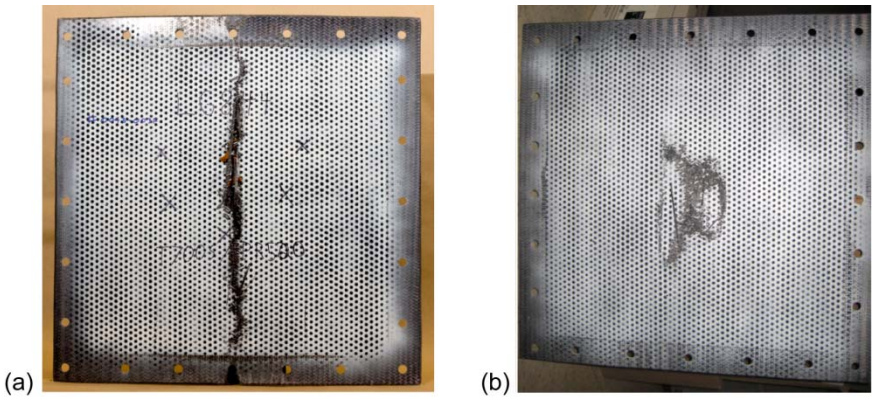

Figure 21.—T700S/PR520 panels after impact. (a) Impact at 194 m/s (637 ft/s). (b) Impact at 230 m/s (756 ft/s).

from the high-speed video showing first fiber failure, growth of the initial damage area, and finally crack initiation in the vertical direction leading to penetration by the projectile. Pictures of penetrated T700S/PR520 panels after testing at 194 m/s (637 ft/s) and 230 m/s (756 ft/s) are shown in Figure 21. The vertical propagation of the crack for the panel tested at 194 m/s (637 ft/s) is not typical of most other material systems that have been tested. The panel tested at 230 m/s (756 ft/s) panel does show some crack propagation along the bias fiber directions, which is a more common mode of failure for other material systems. The different failure modes observed for different materials and for the same material at different test velocities cannot be simulated using current simulation methods. The remainder of this report discusses approaches that are being developed to improve the simulation capability.

Impact Simulation

For this work, the transient dynamic finite element code LS–DYNA (Ref. 18) was utilized. Early attempts to simulate the impact tests described in the previous section used effective properties as the input to the finite element code. The braid architecture was not explicitly modeled. Instead, the material was modeled as an orthotropic material with a set of smeared, homogenized properties. A simulation of an impact test on a flat plate with homogenized material properties for a [0°/+60°/–60°] braided composite is shown in Figure 22.

In Figure 22, failure initiates at the center of the panel, and cracks then propagate equally in the vertical and horizontal directions. The deflection of the panel up to the point of failure correlated well with experiments; however, neither the onset of damage or the crack pattern could be simulated. The penetration threshold for a specific material could be simulated by adjusting input properties or numerical parameters within code. However, there was no systematic way to set the material properties and model parameters such that the penetration threshold for a range of different materials could be simulated. Because homogenized material properties were used in the analysis, the crack pattern in Figure 22 is determined by the panel geometry. Experimental results for panels made from many different material systems indicated that cracks most often follow one of the braid fiber directions. In an attempt to simulate this directionality of crack propagation, Cheng (Ref. 17) developed a method to represent the braid architecture within a shell element by assigning suitable properties to integration points within the elements. In his approach the braid unit cell is discretized into a series of parallel laminated composites using a method to be described below. Results of a panel impact simulation using this approach is shown in Figure 23.

In Figure 23 failure initiates at the center of the panel. A crack first grows for a short distance along the direction of the 0° fibers then turns to propagate along the ±60° fiber directions. This behavior is close to that observed in experiments with some material systems. However, the model was not able to simulate

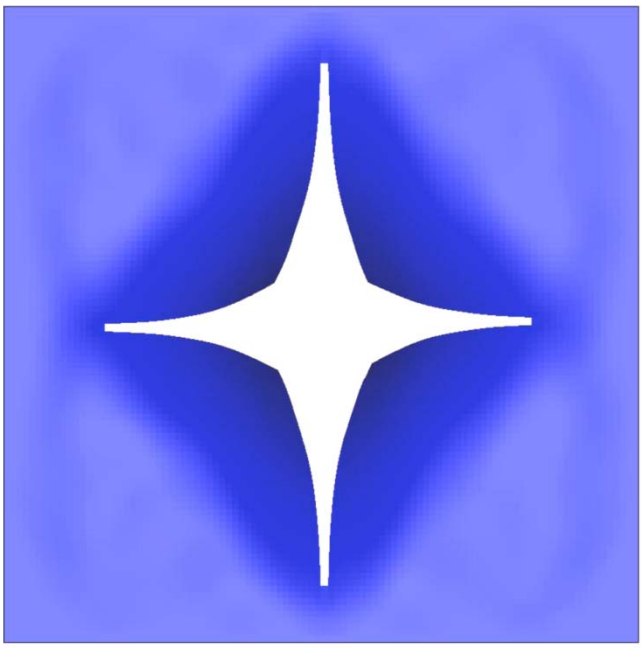

Figure 22.—Simulation of panel impact using homogenized material properties to represent triaxial braid architecture.

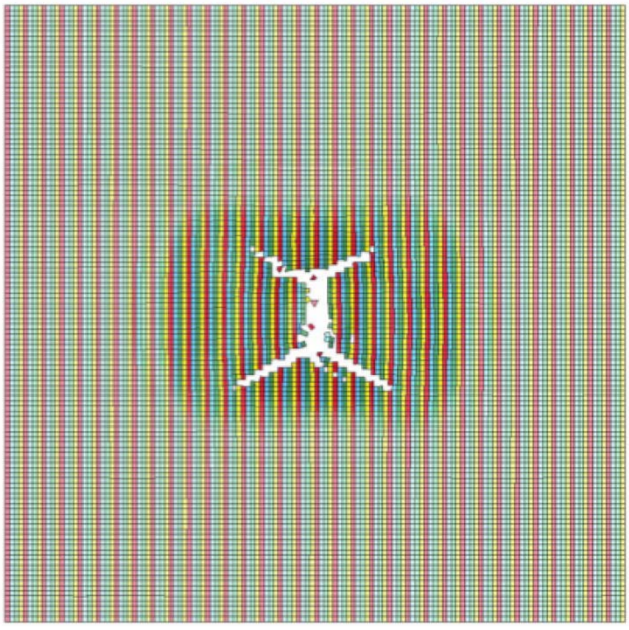

Figure 23.—Simulation of panel impact using discretization approach to represent braid architecture.

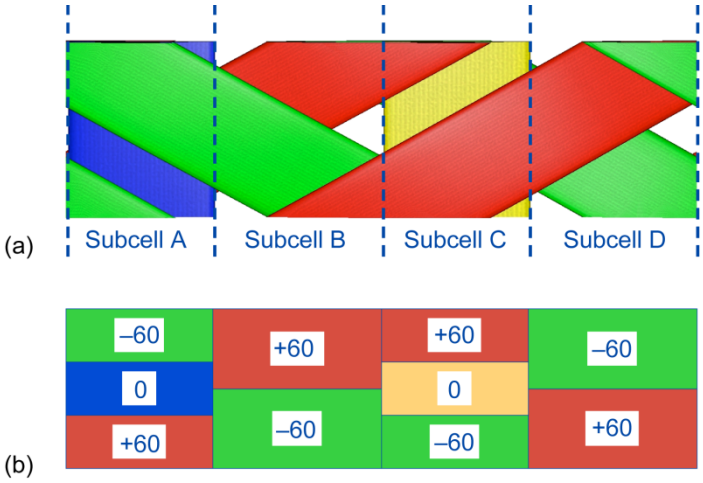

Figure 24.—Schematic of triaxial braid unit cell showing discretization into four subcells. (a) Top view of braid architecture. (b) Edge view of shell elements representing braid architecture.

the wide range of crack patterns observed experimentally. Correlations with the measured penetration threshold could be made by adjusting material properties and other parameters used in the analysis, but prediction of experimental results was not possible. The method described in the remainder of this section builds on the approach developed by Cheng. An approach for simulating a multilayer braided composite is presented, and a systematic method for utilizing experimentally measured material properties in the simulations is described.

A unit cell of the triaxial braided preform is shown in Figure 24. A top view of the braid architecture is shown in Figure 24(a), and an edge view illustrating the shell elements is shown in Figure 24(b). In the schematic, –60º fibers are green, 0º fibers are blue or yellow, and +60º fibers are red. For the present work, the unit cell is subdivided into four parallel subcells, as shown in the figure. For the model, each subcell is approximated to be a laminated composite composed of a stack of fiber bundles at various orientations that are determined by the braid architecture. Subcell A is modeled as a [+60°/0°/–60°] composite (bottom layer listed first). Subcell B is modeled as a [–60°/+60°] composite, subcell C is modeled as a [–60°/0°/+60°] composite, and subcell D is modeled as a [+60°/–60°] composite.

The composites examined in this study were made using six layers of braided preforms. The axial (0°) fibers in each layer were aligned, but the lateral position of axial fibers in each layer was random. As a result, axial fibers in the various layers are not located directly on top of each other. Instead, the axial fiber location in each layer is shifted in a random way relative to the location of axial fiber in the layers above and below. In generating the finite element model for the full six-layer composite, this behavior was approximated by shifting each layer of fibers by one subcell to the left in the full model. A schematic of the full finite element model is shown in Figure 25, where subcell A is pink, subcell B is blue, subcell C is green, and subcell D is yellow. The fiber shifting can be observed in this schematic. For example, in the top layer subcell D is the rightmost subcell. In the second layer subcell D is the second from the right subcell, and so forth.

Each subcell in Figure 25 has 15 layers of fibers, which allows each layer to be given a constant thickness. The difference in size between the 24k axial tows and 12k bias tows was accounted for in the finite element model by weighting the axial layers twice the amount of the bias layers. Related to this, in actuality the +60° and –60° plies in subcells B and D in the one-layer model would have a lower fiber volume ratio than the 0, +60° and –60° plies in subcells A and C, assuming that each subcell has a constant thickness. By incorporating the fiber shifting, the overall fiber volume ratio within each subcell is constant. Also, with this fiber layup, each subcell is a balanced composite, which eliminates the shear

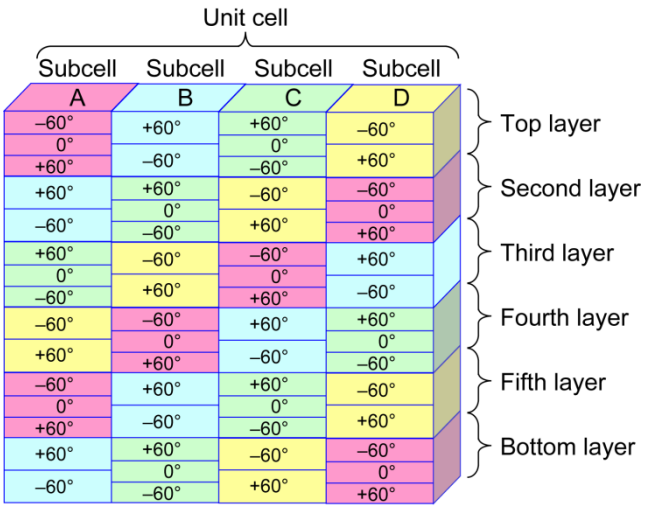

Figure 25.—Schematic of subcell discretization of six-layer triaxial braided composite.

coupling terms within the stiffness matrix. This is useful for back-calculating the equivalent unidirectional properties to be described later. By incorporating the fiber shifting within the finite element model, each subcell will have 0° fibers, +60° fibers, and –60° fibers. In the original configuration, subcells B and D would not have 0° fibers, which might lead to them being overly weak in the axial direction.

Constitutive Model Overview

The material model that is used for these analyses is a continuum damage mechanics-based model for unidirectional composites, based on a theory developed by Matzenmiller, et al. (Ref. 27), that is implemented in LS–DYNA as MAT_58. For this material model, the required input stiffness parameters include the unidirectional-ply-level axial and transverse modulus, in-plane shear modulus, and the in-plane Poisson's ratio. The unidirectional-ply-level strength data that is required includes the axial tensile and axial compressive failure stress and failure strain, the transverse tensile and transverse compressive failure stress and failure strain, and the in-plane shear failure stress and failure strain. The stiffness values are used by the material model to simulate the initial linear portion of the composite response. The ply-level strength and ultimate strain values are used to determine the nonlinear portion of the material response and to determine how the damage parameters used as internal variables within the material model evolve over the loading cycle. Furthermore, the user is allowed to specify a "stress limiting factor" in the longitudinal and/or transverse directions. If the value of the stress limiting factor is set to zero, the failure stress value is assumed to occur at the specified failure strain, and the material model then "connects the dots" (including enforcing any required material nonlinearity) in order to create the best-fit stress strain curve that accounts for the specified stiffness and strength values. If the stress limiting factor is set to one, the stress-strain curve of the composite is assumed to increase linearly until the maximum strength value is reached. At that point, the material is assumed to act as if it were a perfectly plastic material, with the strain in the specified direction, increasing with no increase in stress until such point as the specified strain level is reached, at which point material failure is assumed to occur.

The properties required by the model described above are the properties of the lamina (individual fiber bundles plus a portion of the surrounding resin material). A fundamental problem in the analysis of textile composites is that the lamina properties are not known and cannot be directly measured. Attempts can be made to fabricate unidirectional laminates using the same fiber tows that are used to make the preform. This approach is often not easy to accomplish, and the properties of the unidirectional lamina could be different from the properties of the fiber tows within the textile composite because of processing differences. For these reasons, a method was chosen that utilizes a micromechanics approach to calculate

the lamina properties from experimental data obtained on the braided composite. Although there are also some limitations using this approach, the experimental requirements are simplified, and the calculated lamina properties represent the in situ properties of fiber bundles within the braided composite. The experimental methods described earlier in this report provide the full set of data needed for the model, including guidance on how to specify the stress limiting factors mentioned earlier.

Determination of Material Properties

For both the stiffness and strength properties, test data from coupon tests on the braided composite are utilized to back-calculate the equivalent unidirectional composite properties.

Stiffness Properties

To back-calculate the stiffness properties, first the geometry of a coupon-level transverse tensile test was considered, where the axial fibers are oriented perpendicular to the applied load. A schematic of a test of this type is shown in Figure 26. In this figure, the four subcells of the unit cell are oriented perpendicular to the applied load.

Several assumptions were applied in the model development. The applied load was assumed to be equally divided between all of the braid layers and between each of the unit cells along the width of the composite specimen. Furthermore, by assuming that the common assumptions of classical laminate theory were valid for each of the subcells, the axial and transverse strains for each subcell were assumed to be constant throughout the thickness of the subcell, and the strains measured on the outer surface of the composite were assumed to be the strains throughout each of the layers of the subcell. Therefore, only the single-layer unit cell (Fig. 24) was utilized in the analysis. Each subcell was assumed to have a uniform fiber volume ratio to simplify the analysis, even though subcells B and D most likely have a lower fiber volume fraction than subcells A and C. It is recognized that the fiber volume within subcells needs to be more accurately represented, and current efforts to improve the model are addressing this issue. Each subcell was assumed to have a homogenized average strain (i.e., the strain between subcells could vary, but the strain within a subcell was assumed to be constant). Only in-plane loadings were considered, and in-plane normal-shear couplings were neglected (since the full six-layer subcells were approximated as balanced composites). Even though the composite layups were antisymmetric, tension-bending coupling was neglected in order to simplify the analysis. This assumption was verified by the lack of any bending detected in the full-field strain measurements. For the transverse loading condition and the specified geometry, the applied load in each subcell in the loading direction was assumed to be equal (isostress type of assumption), and the volume average of the applied loads perpendicular to the loading direction in each of the subcells was assumed to be zero.

By utilizing these assumptions in combination with the assumptions and methods of classical lamination theory, a series of equations was generated that relate the applied global stress for the composite coupon (and thus the unit cell) and the subcell-level axial and transverse strains (determined from the experimental data using methods to be described below) in terms of the unidirectional-ply-level stiffness properties. To have enough equations to match all of the unknowns, the geometry of an axial tensile test was also examined (see Fig. 27 for a schematic).

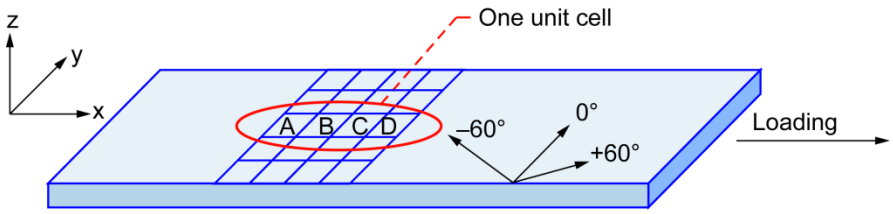

Figure 26.—Schematic of transverse tensile test used for determination of stiffness properties of unidirectional composite.

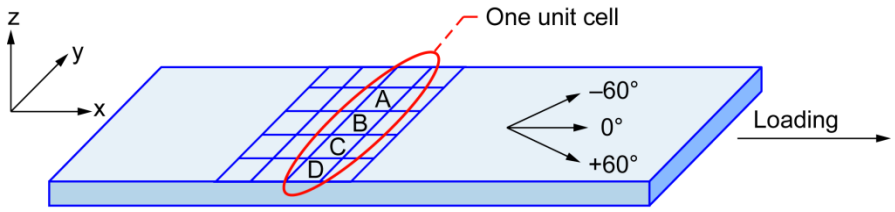

Figure 27.—Schematic of axial tensile test used for determination of stiffness properties of unidirectional composite.

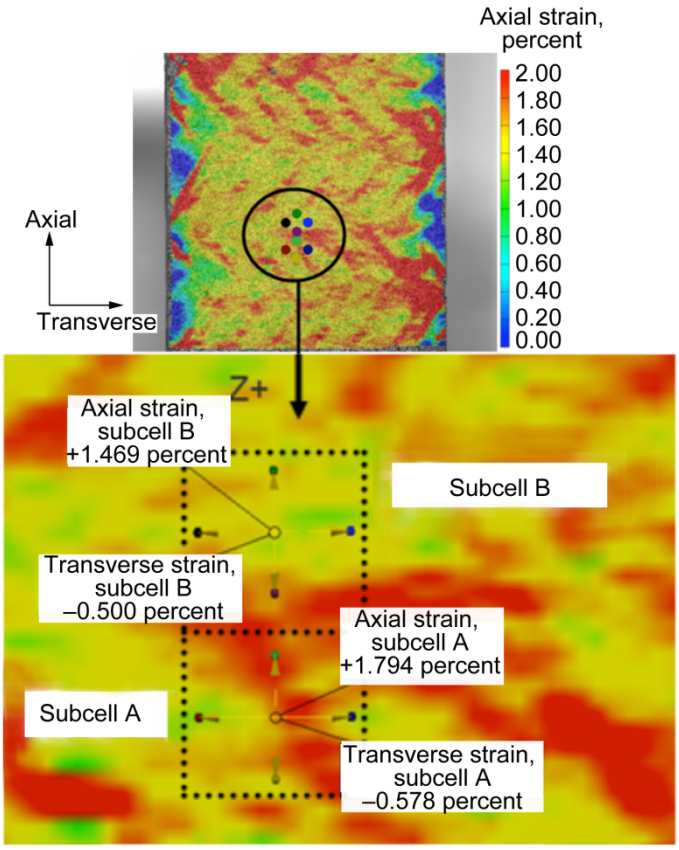

Figure 28.—Optical strain map of local subcell axial strains (in a transverse tensile test) used to determine average subcell strains for determination of unidirectional composite stiffness properties.

In this case, the unit cell and subcells were aligned in the direction of the applied load. The volume average of the load in the loading direction in each of the subcells was assumed to be equal to the global applied load for the unit cell, and the load perpendicular to the loading direction in each of the subcells was assumed to be zero. Once again, by combining these assumptions with classical laminate theory, a series of equations relating the global applied stress, the subcell-level axial and transverse strains, and the effective unidirectional-ply-level properties was obtained.

To apply these equations, the unit-cell-level stresses and the subcell-level strains were assumed to be the known values, and the effective ply-level unidirectional material properties were assumed to be the unknown values. The results from the axial tension and transverse tension were applied independently; that is, stress values from axial tension tests were paired with axial and transverse strain values from axial tension tests, and stress values and axial and transverse strain values from transverse tension tests were linked. To determine the unit-cell-level stresses, a stress value from the initial linear portion of the stress

strain curve was identified, and divided by the number of layers in the composite and again by the number of unit cells in the width of the composite specimen to obtain the average stress in the unit cell. The full-field strain was examined to determine the average strain within regions corresponding to specific subcell locations. An example is shown in Figure 28. The braid architecture can be seen in the upper picture in Figure 28. Regions corresponding to specific subcells can be identified. The average strain in these regions is measured by tracking points near the edge of the region. The points used to measure axial and transverse strains in two subcells are shown in Figure 28. The upper picture shows the locations of these points with respect to the braid architecture, while the lower picture shows a closeup view of the strain field within the subcells. Strain values from multiple unit cells and subcells were measured and averaged. Global stress (and corresponding subcell strain) values were determined from several locations in the linear portion of the axial and transverse stress-strain curves, with their values being applied to the equations. The corresponding computed property values were then averaged in order to obtain average values of the unidirectional-ply-level properties.

Strength Properties

The unidirectional strength values were also determined from the results of coupon tests on the braided material. The assumption was made that in an axial tensile test the load is primarily carried by the axial fibers, with the bias fibers making relatively small contributions. As a result, the axial failure stress and axial failure strain observed for the braided composite were assumed to be equal to the equivalent ply-level unidirectional axial failure stress and axial failure strain. This introduces a small error into the material property calculations that can be corrected in future work.

The strain field measured during axial compression tests was nearly uniform throughout the gage section with little effect of the braid architecture (see Fig. 3(a)). The compressive strains in the axial fibers were therefore assumed to be equal to the global compressive strains in the composite. The compressive stress in the axial fibers was assumed to be equal to the global compressive stress. Therefore, the unidirectional compressive failure stress and failure strain were set equal to the measured global compressive failure stress and failure strain. Even though the compressive stress-strain curves had a significant amount of nonlinearity (see Fig. 3(c)) near the end of the loading curve, and almost resembled a “perfectly plastic” response, the stress limiting factor was still set to zero. This parameter could lead to an underprediction of the compressive response at strains less than the failure strain.

To determine the equivalent transverse compressive failure stress and failure strain, once again the observation was made that during a transverse compression test, the compressive strains are relatively uniform throughout the gage section, indicating that the compressive strain (and by extension the compressive stress) for the axial fibers are equal to the compressive stress and strain for the braided composite. Therefore, once again the equivalent unidirectional transverse compressive failure stress and failure strain were set equal to the transverse compressive failure stress and failure strain for the braided composite. It is recognized that a more detailed analysis of the actual stress within the transverse fiber bundle will be needed for future refinement of the model.

To determine the equivalent transverse tensile failure stress of the unidirectional composite, the transverse tensile test data from the braided composites could not be used directly since in a transverse tension test, unlike in an axial tension test, the bias fibers significantly contribute to the global response of the composite. The lowest global transverse stress at which fiber splitting occurred (see Fig. 10) was used as the transverse failure stress for the unidirectional composite. Again, it is recognized that a more detailed analysis of the actual stress within the transverse fiber bundle is needed. The local transverse strain at the site of a fiber bundle split could be measured directly (see Fig. 10 and related discussion in the “Tensile Test Results” section). The strain at which fiber bundle splitting occurred was taken to be the transverse tensile failure strain for the unidirectional lamina. In a unidirectional composite complete failure occurs when the transverse failure stress is reached. In a braided composite the fiber bundles are constrained by adjacent fiber bundles, so multiple splits occur within a fiber bundle before complete failure of the composite. To account for this behavior, the stress limiting factor in the transverse direction

was set equal to one. This allows the material to act as if it were a perfectly plastic material after the onset of fiber bundle splitting.

To compute the shear failure stress and the shear failure strain, the assumption was made that under pure shear loading, the shear stress and shear strain in every layer in all of the subcells was equal to the global shear stress and shear strain. Therefore, the equivalent unidirectional shear strength and shear failure strain was assumed to be equal to the shear failure stress and shear failure strain measured for the composite.

Simulation of Quasi-Static Tension Tests

A series of simulations were conducted to evaluate the analysis methods described above. First, the quasi-static axial and transverse tensile tests on the T700S/PR520 material were simulated. The finite element meshes are shown in Figure 29. The finite element model for the axial tension test was 20.32 cm (8.0 in.) long and 3.56 cm (1.40 in.) wide and had 369 nodes and 320 shell elements. The model for the transverse tensile test was 30.48 cm (12 in.) long and 3.56 cm (1.40 in.) wide and had 522 nodes and 476 elements.

The fixed end of the model was constrained in all three displacement and rotation directions. The loading was displacement controlled at the rate of 0.0635 cm/s (0.025 in./s), which was consistent with the test conditions. Each subcell was modeled as a shell element. In the figure, the red elements represent subcell A, the blue elements represent subcell B, the green elements represent subcell C, and the yellow elements represent subcell D. Each subcell is modeled using an individual shell element. This allows the braid architecture to be explicitly modeled within the finite element mesh. The unit cell orientations for both of the modeling conditions are highlighted for reference. In the axial test simulation the unit cell is oriented perpendicular to the direction of the applied load. In the transverse test simulation the unit cell is oriented parallel to the direction of the applied load.

Tensile stress versus strain curves were generated for the T700S/PR520 material in both the axial and transverse directions. The material properties that were used for the analysis are shown in Table IV. Failure was deemed to occur when all of the elements in a row failed. The element failure occurred nearly simultaneously in the simulations, leading to a fairly abrupt ultimate failure. The resulting stress-strain curves are shown in Figure 30.

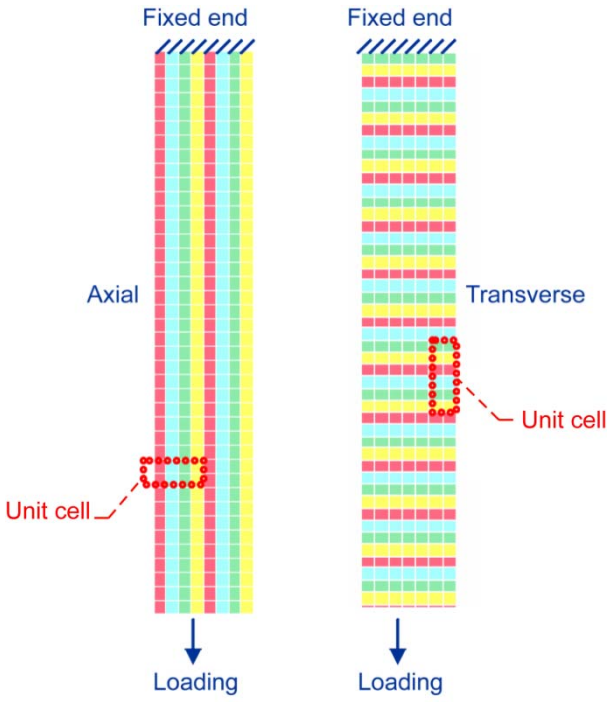

Figure 29.—Finite element models of T700S/PR520 coupons for tensile tests. (a) Axial. (b) Transverse.

TABLE IV.—EQUIVALENT UNIDIRECTIONAL MATERIAL PROPERTIES OF T700/PR520 TRIAXIAL BRAID COMPOSITE USED FOR SIMULATIONS[a]

Axial modulus EA, GPa (Msi)	51.37 (7.45)
Transverse modulus EB, GPa (Msi)	25.03 (3.63)
In-plane shear modulus GAB, GPa (Msi)	18.96 (2.75)
In-plane Poisson's ratio PRBA	0.071
Axial tensile failure strain E11T	0.0216
Axial compressive failure strain E11C	0.018
Transverse tensile failure strain E22T	0.0168
Transverse compressive failure strain E22C	0.011
In-plane shear failure strain GMS	0.024
Axial tensile stress at failure XT, MPa (ksi)	1044.59 (151.5)
Axial compressive stress at failure XC, MPa (ksi)	377.09 (54.69)
Transverse tensile stress at failure YT, MPa (ksi)	361.99 (52.5)
Transverse compressive stress at failure YC, MPa (ksi)	344.75 (50.0)
In-plane shear stress at failure SC, MPa (ksi)	307.31 (44.57)
Stress-limiting parameter for axial tension SLIMT1	0
Stress-limiting parameter for transverse tension SLIMT2	1
Stress-limiting parameter for axial compression SLIMC1	0
Stress-limiting parameter for transverse compression SLIMC2	0
Stress-limiting parameter for shear SLIMS	0

[a]Symbols are those used by LS–DYNA code (Ref. 18).

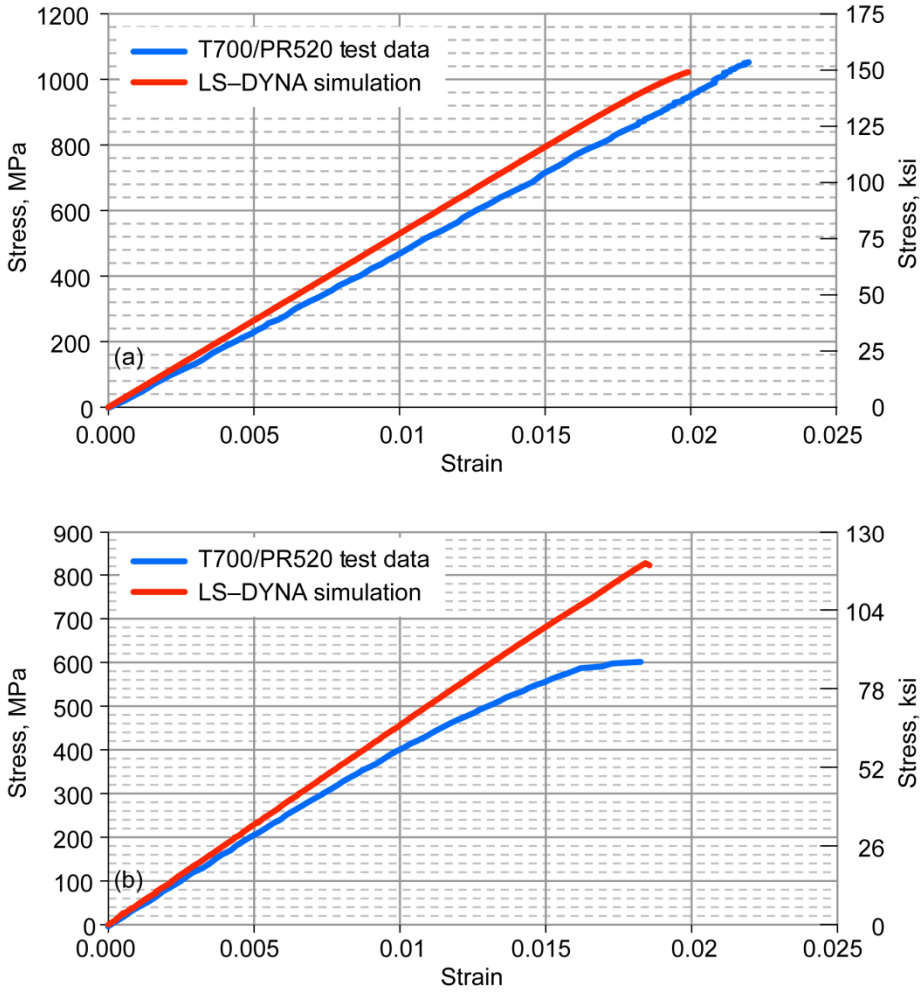

Figure 30.—Experimental and simulated stress-strain response for T700S/PR520 triaxial braided composite during tensile coupon tests. (a) Axial. (b) Transverse.

In both the axial and transverse tests, the correlation of the computed modulus to the actual modulus was reasonably good. The fact that the axial tensile specimen exhibited a linear response until failure was captured by the simulations. The simulated axial tensile strength of the specimen also was closely correlated with the experimental results. However, the ultimate strength of the transverse tensile specimen was significantly overpredicted, and the simulated response of the transverse tensile test was much more linear than observed in the experiments. One possible cause for the discrepancy is related to the fact that in the transverse tensile tests all of the bias fibers are not gripped, which may lead to an overly weak response. Further studies need to be made on whether the observed discrepancies are caused by limitations in the experimental techniques or limitations imposed by the assumptions used in the analysis method.

Simulation of Impact Tests

Simulations of the impact tests of the T700S/PR520 material described earlier in the report were conducted. To simulate the flat panels used in the impact tests, a finite element mesh 0.6096 m (24 in.) wide, 0.6096 m (24 in.) long, and 0.3175 cm (0.125 in.) thick with 16 320 shell elements was used. The finite element mesh of the panel is shown in Figure 31.

The four sides of the panel were constrained in all three displacement and all three rotation directions. Because the gelatin is a low-strength, low-stiffness, and high-flow material, it was modeled as a fluid with a specified pressure-volume relation. The material equation-of-state relationship was also used for simulation of the shock wave at initial contact. To account for the extreme deformation of the gelatin during impact, the gelatin geometry was implemented into an Arbitrary Lagrangian Eularian (ALE) mesh, which allowed the gelatin to flow freely and exhibit large deformations. This model was able to simulate the large deformation of the projectile shown in Figure 14. Further details about the gelatin model can be found in Reference 17. The model parameters have been adjusted in part by correlation with results of previous impact tests on composite panels. This is a limitation on the predictive capability of the current simulation method, and improved projectile models are being considered. The gelatin was modeled using 41 040 solid elements. Simulations were run for various impact velocities above and below the penetration threshold. The penetration threshold in the simulations was defined as the velocity at which any element completely failed, with all of the integration points failing. The model predicted penetration taking place at an impact velocity of 191 m/sec (627 ft/s), which agreed well with the experimentally determined velocity threshold of 194 m/sec (637 ft/s).

For this case of impact penetration, the initiation and progression of damage was also compared with the experimental results. The experimental and predicted damage patterns are shown in Figure 32.

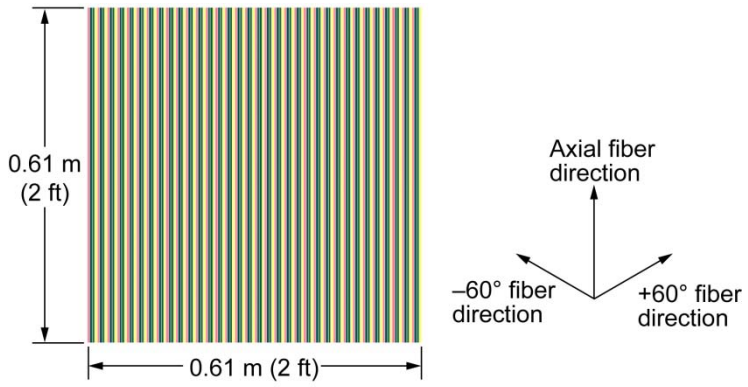

Figure 31.—Finite element mesh of triaxial-braided T700/PR520 flat plate utilized in simulation of impact tests.

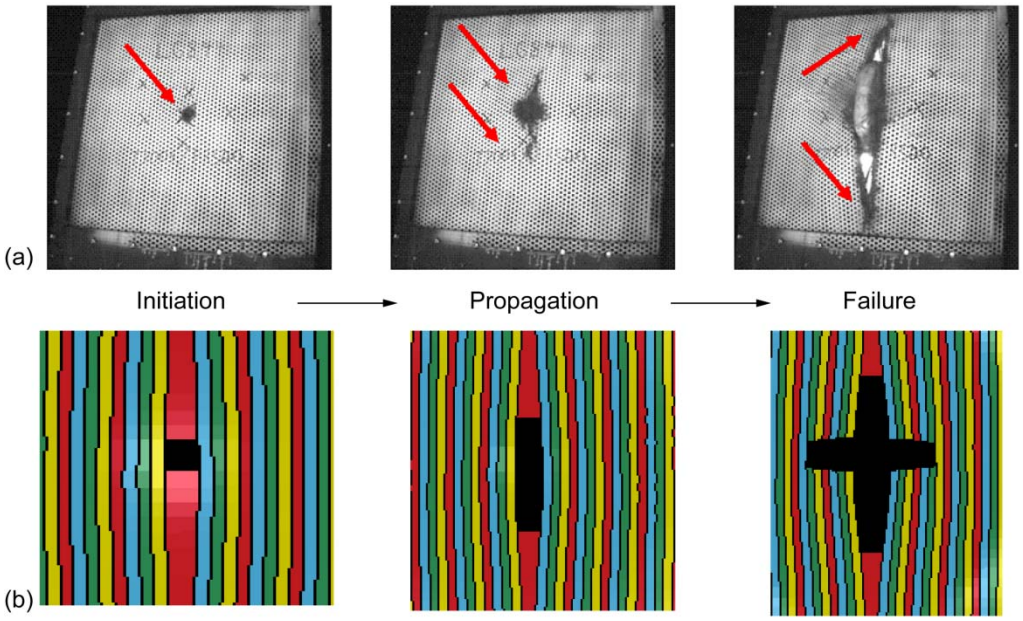

Figure 32.—The progression of failure in T700/PR520 material system at 194 m/s. (a) Test results. (b) Simulation results.

In the experiments the damage initiates in the middle of the panel and propagates in the vertical direction parallel with the axial fibers. The simulation captured the failure initiation and the initial propagation of damage. However, transverse cracks occurred later in the simulation. The damage pattern in the simulations is similar to that shown for a homogeneous material in Figure 22. This is probably caused by the assumption of constant fiber volume fraction in all subcells. This can best be explained by examining Figure 24. The constant fiber volume assumption artificially strengthens the bias fibers in subcells B and D. Because of the fiber angles within these subcells, the increased fiber strength would suppress crack propagation along the bias fiber direction and the axial direction to a greater extent than along the transverse direction. An initial set of parametric studies indicated that the model in its current form cannot simulate experiments in which cracks grow along bias fiber directions. In the simulations performed by Cheng (see Fig. 23), it was possible to simulate crack growth in bias fiber directions by reducing the fiber volume fraction in subcells B and D and adjusting other model parameters. This suggests that it should be possible to better simulate crack propagation using the new model as the model is refined. If this can be achieved, the advantage of the new approach is that the fiber architecture in a multilayer laminate can be better represented, and there is a clear methodology for obtaining material properties from experimental data and setting parameters (such as the stress limiting factors) to reflect actual material behavior. Although damage progression in the impact tests was not adequately simulated, the damage initiation that leads to failure was simulated. In addition, the simulations correlate well with the overall panel deformation.

Conclusions

The coordinated test and analysis method presented in the report appears to be a promising approach for simulating ballistic impact of triaxial braided composite materials. The analysis method is computationally efficient and uses data directly measured on coupon specimens made with the triaxial braided material. Damage initiation and initial propagation of the crack during impact were simulated for the material system presented in this report. Data used in the analysis were obtained using standard composite test methods augmented by full-field strain measurements. Several improvements are needed to make the simulation method more accurate and more capable of representing the wide range of failure

modes that have been observed for different material systems. Continued work is needed to eliminate edge effects and ensure uniform deformation in the gage section of tensile test specimens. Data from tests that involve multiaxial loading, out-of-plane bending, and high strain rates would improve material characterization and provide for better model validation. The methods used to acquire and analyze full-field strain data must be standardized for both quasi-static and impact tests. Ongoing refinements of the micromechanics analysis will yield more realistic estimates of the local fiber bundle stresses as a function of the global applied stress. These refined calculations could be used to provide more realistic values for the composite strength properties used in the model. The simulation approach described in this report should be a suitable framework for implementation of these improvements as the newer information becomes available.

References

1. Standard Guide for Testing Polymer Matrix Composite Materials. ASTM D4762, Book of Standards Vol. 15.03, 2008.
2. Standard Guide for Testing Fabric-Reinforced "Textile" Composite Materials. ASTM D6856, Book of Standards Vol. 15.03, 2008.
3. Defense Technical Information Center: Composite Materials Handbook. Vol. 1, DOD–MIL–HDBK–17/1F, ASTM International, West Conshohocken, PA, 2002.
4. Tomblin, John S.; Ng, Yeow C.; and Raju, K.S.: Material Qualification and Equivalency for Polymer Matrix Composite Material Systems. DOT/FAA/AR–00/47, 2001.
5. Tomblin, J., et al.: Material Qualification Methodology for 2×2 Biaxially Braided RTM Composite Material Systems. AGATE–WP3.3–033048–116, 2001.
6. Masters, John E., et al.: The Effects of Specimen Width on Tensile Properties of Triaxially Braided Textile Composites. NASA CP–3178, vol. 1, pt. 2, 1993, pp. 523–536.
7. Masters, John E.: Strain Gage Selection Criteria for Textile Composite Materials. NASA CR–198286, 1996.
8. Masters, John E.; and Portanova, Marc A.: Standard Test Methods for Textile Composites. NASA CR– 4751, 1996.
9. Masters, John E.; and Ifju, Peter G.: Phenomenological Study of Triaxially Braided Textile Composites Loaded in Tension. Compos. Sci. Technol., vol. 56, no. 3, 1996, pp. 347–358.
10. Littell, Justin: The Experimental and Analytical Characterization of the Macromechanical Response for Triaxial Braided Composite Materials. Ph.D. Dissertation, Univ. of Akron, 2008. http://www.ohiolink.edu/etd/view.cgi?acc_num=akron1224164770 Accessed June 3, 2009.
11. Chou, T.-W.; and Ishikawa, T.: Analysis and Modeling of Two-Dimensional Fabric Composites. Textile Structural Composites, Composite Materials Series, Tsu-Wei Chou and Frank K. Ko, eds., vol. 3, ch. 7, Elsevier, Amsterdam, 1989, p. 209.
12. Naik, N.K.; and Shembekar, P.S.: Elastic Behavior of Woven Fabric Composites: I-Lamina Analysis. J. Compos. Mater., vol. 26, no. 15, 1992, pp. 2196–2225.
13. Pastore, Christopher; and Gowayed, Yasser A.: Self-Consistent Fabric Geometry Model: Modification and Application of a Fabric Geometry Model to Predict the Elastic Properties of Textile Composites. J. Compos. Technol. Res., vol. 16, no. 1, 1994, pp. 32–36.
14. Byun, Joon-Hyung: The Analytical Characterization of 2–D Braided Textile Composites. Compos. Sci. Technol., vol. 60, no. 5, 2000, pp. 705–716.
15. Tanov, R.; and Tabiei, A.: Computationally Efficient Micromechanical Models for Woven Fabric Composite Elastic Moduli. J. Appl. Mech. Trans. ASME, vol. 68, no. 4, 2001, pp. 553–560.
16. Bednarcyk, Brett A.; and Arnold, Steven M.: Modeling Woven Polymer Matrix Composites With MAC/GMC. NASA/CR—2000-210370, 2000.
17. Cheng, Jingyun: Material Modeling of Strain Rate Dependent Polymer and 2D Tri-Axially Braided Composites. Ph.D. Dissertation, Univ. of Akron, 2006.
18. Livermore Software Technology Corp.: LS–DYNA Keyword User's Manual. Vol. I, version 971, 2007.

19. Standard Test Method for Tensile Properties of Polymer Matrix Composites. ASTM D3039, Book of Standards Vol. 15.03, 2000.
20. Standard Test Method for Compressive Properties of Polymer Matrix Composite Materials With Unsupported Gage Section by Shear Loading. ASTM D3410, Book of Standards Vol. 15.03, 2008.
21. Standard Test Method for Shear Properties of Composite Materials by the V-Notched Beam Method. ASTM D5379, Book of Standards Vol. 15.03, 2005.
22. Standard Test Method for Shear Properties of Composite Materials by V-Notched Rail Shear Method. ASTM D7078, Book of Standards Vol. 15.03, 2005.
23. Adams, Daniel O., et al: The V-Notched Rail Shear Test. J. Compos. Mater., vol. 41, no. 3, 2007, pp. 281–297.
24. Roberts, Gary D., et al.: Characterization of Triaxial Braided Composite Material Properties for Impact Simulation. Presented at the American Helicopter Society 65th Annual Forum and Technology Display, Grapevine, TX, 2009.
25. Bowman, C.L., et al.: Mechanical Properties of Triaxial Braided Carbon/Epoxy Composites. Presented at the 35th International SAMPE Technical Conference—Materials and Processing: Enabling Flight…Our Legacy and Future, Dayton, OH, 2003.
26. Roberts, Gary D., et al.: Ballistic Impact of Braided Composites With a Soft Projectile. J. Aerosp. Eng., vol. 18, no. 1, 2005, pp. 3–7.
27. Matzenmiller, A.; Lubliner, J.; and Taylor, R.L.: Constitutive Model for Anisotropic Damage in Fiber-Composites. Mech. Mater., vol. 20, no. 2, 1995, pp. 125–152.22.

REPORT DOCUMENTATION PAGE		Form Approved OMB No. 0704-0188

1. REPORT DATE *(DD-MM-YYYY)*	2. REPORT TYPE	3. DATES COVERED *(From - To)*
01-09-2009	Technical Memorandum	

4. TITLE AND SUBTITLE
Characterization of Triaxial Braided Composite Material Properties for Impact Simulation

5a. CONTRACT NUMBER

5b. GRANT NUMBER

5c. PROGRAM ELEMENT NUMBER

6. AUTHOR(S)
Roberts, Gary, D.; Goldberg, Robert, K.; Binienda, Wieslaw, K.; Arnold, William, A.; Littell, Justin, D.; Kohlman, Lee, W.

5d. PROJECT NUMBER

5e. TASK NUMBER

5f. WORK UNIT NUMBER
WBS 877868.02.07.03.05.03

7. PERFORMING ORGANIZATION NAME(S) AND ADDRESS(ES)
National Aeronautics and Space Administration
John H. Glenn Research Center at Lewis Field
Cleveland, Ohio 44135-3191

8. PERFORMING ORGANIZATION REPORT NUMBER
E-17002

9. SPONSORING/MONITORING AGENCY NAME(S) AND ADDRESS(ES)
National Aeronautics and Space Administration
Washington, DC 20546-0001

10. SPONSORING/MONITOR'S ACRONYM(S)
NASA

11. SPONSORING/MONITORING REPORT NUMBER
NASA/TM-2009-215660

12. DISTRIBUTION/AVAILABILITY STATEMENT
Unclassified-Unlimited
Subject Categories: 24, 39, and 05
Available electronically at http://gltrs.grc.nasa.gov
This publication is available from the NASA Center for AeroSpace Information, 443-757-5802

13. SUPPLEMENTARY NOTES

14. ABSTRACT
The reliability of impact simulations for aircraft components made with triaxial braided carbon fiber composites is currently limited by inadequate material property data and lack of validated material models for analysis. Improvements to standard quasi-static test methods are needed to account for the large unit cell size and localized damage within the unit cell. The deformation and damage of a triaxial braided composite material was examined using standard quasi-static in-plane tension, compression, and shear tests. Some modifications to standard test specimen geometries are suggested, and methods for measuring the local strain at the onset of failure within the braid unit cell are presented. Deformation and damage at higher strain rates is examined using ballistic impact tests on 61- by 61- by 3.2-mm (24- by 24- by 0.125-in.) composite panels. Digital image correlation techniques were used to examine full-field deformation and damage during both quasi-static and impact tests. An impact analysis method is presented that utilizes both local and global deformation and failure information from the quasi-static tests as input for impact simulations. Improvements that are needed in test and analysis methods for better predictive capability are examined.

15. SUBJECT TERMS
Composite materials; Braided composites; Graphite-epoxy composites; Composite structures; Impact tests; Numerical analysis

16. SECURITY CLASSIFICATION OF:			17. LIMITATION OF ABSTRACT	18. NUMBER OF PAGES	19a. NAME OF RESPONSIBLE PERSON
a. REPORT	b. ABSTRACT	c. THIS PAGE			STI Help Desk (email:help@sti.nasa.gov)
U	U	U	UU	40	19b. TELEPHONE NUMBER *(include area code)* 443-757-5802